Monthly Notices
of the
ROYAL ASTRONOMICAL SOCIETY

Mon. Not. R. Astron. Soc. **419,** 3505–3520 (2012) doi:10.1111/j.1365-2966.2011.19993.x

The Herschel Virgo Cluster Survey – VIII. The Bright Galaxy Sample⋆

J. I. Davies,[1]† S. Bianchi,[2] L. Cortese,[3] R. Auld,[1] M. Baes,[4] G. J. Bendo,[5] A. Boselli,[6] L. Ciesla,[6] M. Clemens,[7] E. Corbelli,[2] I. De Looze,[4] S. di Serego Alighieri,[2] J. Fritz,[4] G. Gavazzi,[8] C. Pappalardo,[2] M. Grossi,[9] L. K. Hunt,[2] S. Madden,[10] L. Magrini,[2] M. Pohlen,[1] M. W. L. Smith,[1] J. Verstappen[4] and C. Vlahakis[11]

[1]*School of Physics and Astronomy, Cardiff University, The Parade, Cardiff CF24 3AA*
[2]*INAF-Osservatorio Astrofisico di Arcetri, Largo Enrico Fermi 5, 50125 Firenze, Italy*
[3]*European Southern Observatory, Karl-Schwarzschild Strasse 2, 85748 Garching bei Muenchen, Germany*
[4]*Sterrenkundig Observatorium, Universiteit Gent, KrijgslAAn 281 S9, B-9000 Gent, Belgium*
[5]*Jodrell Bank Centre for Astrophysics, School of Physics and Astronomy, University of Manchester, Oxford Road, Manchester M13 9PL*
[6]*Laboratoire d'Astrophysique de Marseille, UMR 6110 CNRS, 38 rue F. Joliot-Curie, F-13388 Marseille, France*
[7]*INAF-Osservatorio Astronomico di Padova, Vicolo dell'Osservatorio 5, 35122 Padova, Italy*
[8]*Universita' di Milano-Bicocca, piazza della Scienza 3, 20100 Milano, Italy*
[9]*CAAUL, Observatório Astronómico de Lisboa, Universidade de Lisboa, Tapada da Ajuda, 1349-018 Lisboa, Portugal*
[10]*Laboratoire AIM, CEA/DSM - CNRS - Université Paris Diderot, Irfu/Service, Paris, France*
[11]*Departamento de Astronomia, Universidad de Chile, Casilla 36-D, Santiago, Chile*

Accepted 2011 October 11. Received 2011 September 30; in original form 2011 May 19

ABSTRACT

We describe the Herschel Virgo Cluster Survey and the first data that cover the complete survey area (four 4×4 deg^2 regions). We use these data to measure and compare the global far-infrared properties of 78 optically bright galaxies that are selected at 500 μm and detected in all five far-infrared bands. We show that our measurements and calibration are broadly consistent with previous data obtained by the *IRAS*, *ISO*, *Spitzer* and *Planck*. We use SPIRE and PACS photometry data to produce 100-, 160-, 250-, 350- and 500-μm cluster luminosity distributions. These luminosity distributions are not power laws, but 'peaked', with small numbers of both faint and bright galaxies. We measure a cluster 100–500 μm far-infrared luminosity density of $1.6(7.0) \pm 0.2 \times 10^9$ L$_\odot$ Mpc^{-3}. This compares to a cluster 0.4–2.5 μm optical luminosity density of $5.0(20.0) \times 10^9$ L$_\odot$ Mpc^{-3}, some 3.2(2.9) times larger than the far-infrared. A 'typical' photon originates from an optical depth of 0.4 ± 0.1. Most of our sample galaxies are well fitted by a single modified blackbody ($\beta = 2$), leading to a mean dust mass of $\log M_{\rm Dust} = 7.31$ M$_\odot$ and temperature of 20.0 K. We also derive both stellar and atomic hydrogen masses from which we calculate mean values for the star-to-gas (atomic) and gas (atomic)-to-dust mass ratios of 15.1 and 58.2, respectively. Using our derived dust, atomic gas and stellar masses, we estimate cluster mass densities of $8.6(27.8) \times 10^6$, $4.6(13.9) \times 10^8$ and $7.8(29.7) \times 10^9$ M$_\odot$ Mpc^{-3} for dust, atomic gas and stars, respectively. These values are higher than those derived for field galaxies by factors of 39(126), 6(18) and 34(129), respectively. In the above, the luminosity/mass densities are given using the whole sample with the values in brackets using just those galaxies that lie between 17 and 23 Mpc. We provide a data table of flux densities in all the *Herschel* bands for all 78 bright Virgo Cluster galaxies.

Key words: galaxies: clusters: individual: Virgo – galaxies: general – galaxies: ISM.

1 INTRODUCTION

The spectacular number of large diffuse nebulae in the constellation of Virgo has attracted the attention of astronomers for centuries. We now know the nebulae to be galaxies and that they reside in the largest nearby galaxy cluster. The cluster consists of many

⋆*Herschel* is an ESA space observatory with science instruments provided by European-led Principal Investigator consortia and with important participation from NASA.

†E-mail: jid@astro.cf.ac.uk

thousands of galaxies both physically large and small, and because of its proximity ($v \sim 1094\,\mathrm{km\,s^{-1}}$, Binggeli, Tammann & Sandage 1987; $d \sim 17$ Mpc, Gavazzi et al. 1999; $d \sim 16.5$ Mpc, Mei et al. 2007) the largest galaxies subtend some of the biggest angular sizes (∼10 arcmin) in the sky.

These big bright galaxies occupy a relatively small area ($\approx 100\,\mathrm{deg^2}$) and so, over the years, the whole region has been subject to extensive 'survey' observations. Recent surveys range from the X-ray (Boehringer et al. 1994), ultraviolet (Boselli et al. 2011), optical (Virgo Cluster Catalogue, hereinafter VCC, Binggeli, Sandage & Tammann 1985; SDSS, Abazajian et al. 2009; VGVS, Mei et al. 2010), near-infrared (Two-Micron All-Sky Survey, hereinafter 2MASS, Skrutskie et al. 2006; UKIDSS, Warren et al. 2007), far-infrared (*IRAS*, Neugebauer et al. 1984) and 21 cm (ALFALFA, Giovanelli et al. 2005; VIVA, Chung et al. 2009; AGES, Taylor 2010). These extensive large data sets provide us with a unique opportunity to study in detail a large number of galaxies at high spatial resolution.

However, the properties of cluster galaxies may not be typical of galaxies in general. The environment of a galaxy cluster is very different from that of other less densely populated 'field' regions of the Universe. The proximity of other galaxies and the existence of an intergalactic medium means that Virgo Cluster galaxies probably evolve in ways that are in detail quite different from that of field galaxies. For example, in the cluster, the morphological mix of galaxies is quite different from that in the field and many galaxies are observed to be relatively deficient in atomic gas (Haynes & Giovanelli 1984). This deficiency in gas is probably responsible for the observed lower star formation rates (Lewis et al. 2002; Gomez et al. 2003) and the truncation of star-forming discs (Boselli & Gavazzi 2006) seen in cluster galaxies. An understanding of the prime physical processes that influence how a galaxy changes and evolves with time is a primary motivation for the study of galaxies in the nearby Universe, particularly the identification of processes unique to the cluster environment.

Given that the very essence of what a galaxy does is to form stars, and hence convert primordial gas into heavy elements (metals), the fractional mass of these elements compared to the gas is a primary indicator of how far a galaxy has proceeded along its evolutionary path. A major depository of these metals is in the interstellar dust, and an important and outstanding legacy from the hugely successful *IRAS* survey of the 1980s has been the question of determining the total quantity of dust in galaxies. The issue has been outstanding because the *IRAS* with a maximum wavelength of 100 μm measured warm dust in galaxies (generally $T \sim 30+$ K), leading to gas-to-dust mass ratios higher by about a factor of 10 than that observed in our Galaxy (measured by other means, i.e. stellar extinction). They are also much higher than expected using chemical evolution models that predict the fractional mass of dust produced in each generation of stars (Dwek 1998; Edmunds & Eales 1998). The open question since then has been just how much cold dust ($T \leq 20$ K) remains undetected in galaxies and whether this can reconcile our local observations of the Milky Way and the dust-production models.

There have, of course, been other far-infrared space missions since the *IRAS* that have to some extent addressed the cold dust issue. In particular, Tuffs et al. (2002) and Popescu et al. (2002) discuss this, amongst other issues, using bright Virgo Cluster galaxies observed by the *Infra-red Space Observatory* (*ISO*). Other *ISO* observations of individual galaxies which specifically address the cold dust issue have been described by Alton et al. (1998a), Davies et al. (1999), Trewhella et al. (2000), Bendo et al. (2002) and Bendo et al. (2003). The *Spitzer Space Telescope* has also made observations of nearby galaxies at wavelengths at or just beyond that observed by the *IRAS* (out to about 200 μm) with the Spitzer Infrared Nearby Galaxy Survey sample being of particular importance in helping us understand the far-infrared properties of galaxies (Kennicutt et al. 2003).

Both the *ISO* and *Spitzer* have been somewhat limited in what can be inferred about the cold dust issue for three reasons. The first is that the wavelength coverage is not in the critical wavelength region where we expect to detect the signature of cold dust (200–600 μm). The second is that these were not survey telescopes and so they did not provide objectively selected large samples of galaxies for comparative study at the wavelengths of interest. Thirdly, because small quantities of warm dust can swamp the signal from cold dust, it is important to have sufficient spatial resolution to identify regions in the galaxy where cold dust emission is dominant. Although SCUBA observations at 850 μm (Alton et al. 1998b; Bianchi et al. 2000b; Dunne et al. 2000; Vlahakis et al. 2005) have also attempted to address the above issues, with the advent of the *Herschel Space Telescope*, these problems we hope can be solved conclusively.

The observations of Virgo Cluster galaxies described below make use of the unique imaging qualities and sensitivity of *Herschel* at five wavelengths from 100 to 500 μm. With a 3.5-m mirror, the spatial resolution of *Herschel* at these wavelengths ranges from 7 to 35 arcsec, enabling spatially resolved observations of many of the bright galaxies at the distance of Virgo. The Herschel Virgo Cluster Survey (HeViCS) is an approved ESA *Herschel Space Telescope* (Pilbratt et al. 2010) Open Time Key Project. The project has been awarded 286 hours of observing time in parallel mode using tle PACS (Poglitsch et al. 2010) at 100 and 160 μm, and SPIRE (Griffin et al. 2010) at 250, 350 and 500 μm. Eventually, we will map four 4×4 deg^2 regions of the cluster down to the confusion limit in the SPIRE bands. Pre-*Herschel* comparable surveys describing the far-infrared properties of nearby bright galaxies have been described by Soifer et al. (1987), Doyon & Joseph (1989) (*IRAS*), Tuffs et al. (2002) (*ISO*) and Draine et al. (2007) (*Spitzer*).

In this paper, we describe results from an initial data release that covers the entire HeViCS area but using only a quarter of the scans that will constitute the final data set. For this reason, this paper concentrates on the properties of the bright galaxies because these are still detected at high signal-to-noise ratio (S/N) even in these as yet incomplete data. The primary HeViCS science goals using the full depth data include the detection of dust in the intergalactic medium, the extent of cold dust in the outskirts of galaxies, far-infrared luminosity functions, the complete spectral energy distributions (SEDs) of galaxies, the dust content of dwarf ellipticals and irregulars, and a detailed analysis of the dust content of early-type galaxies (for further details, visit http://www.hevics.org).

This paper is an extension of a previous paper (Paper I, Davies et al. 2010), of this series of papers, that considered the properties of the bright galaxies in a single central 4×4 deg^2 HeViCS field. In the other six papers (of this series) on this central field, we have discussed how the cluster environment truncates the dust discs of spiral galaxies (Paper II, Cortese et al. 2010), the dust lifetime in early-type galaxies (Paper III, Clemens et al. 2010), the spiral galaxy dust surface density and temperature distribution (Paper IV, Smith et al. 2010), the properties of metal-poor star-forming dwarf galaxies (Paper V, Grossi et al. 2010), the lack of thermal emission from the elliptical galaxy M87 (Paper VI, Baes et al. 2010), and the far-infrared detection of dwarf elliptical galaxies (Paper VII, De Looze et al. 2010). Another paper (Boselli et al. 2010) discusses the SEDs of HeViCS galaxies together with others observed as part of the Herschel Reference Survey (HRS).

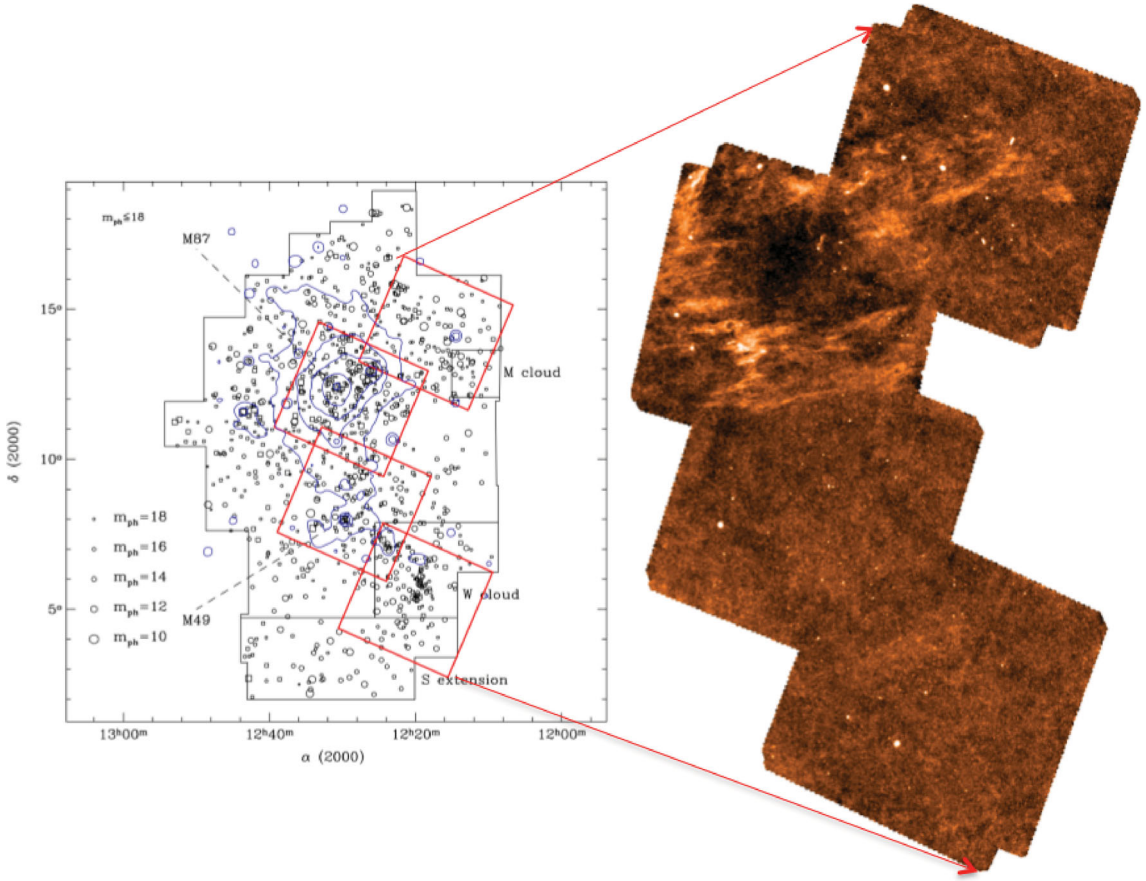

Figure 1. The Virgo Cluster. On the left-hand side is shown the area (∼100 deg^2) observed as part of the Binggeli et al. (1987) survey which led to the VCC of some 2000 galaxies. Each VCC galaxy is marked as a circle. The area (∼64 deg^2) covered by the HeViCS is indicated by the red boxes. X-ray contours as observed by the *ROSAT* are shown in blue (Boehringer et al., 1994). On the right-hand side are the four fields as observed by *Herschel* (SPIRE) at 250 μm. Bright galaxies can be seen as white dots. Prominent on the frames is the emission from the Galactic cirrus.

2 OBSERVATIONS, DATA REDUCTION, OBJECT SELECTION AND CALIBRATION CHECKS

We have obtained ∼64 deg^2 of data over four fields covering a large part of the Virgo Cluster using the SPIRE/PACS parallel scan-map mode (Fig. 1). We use nominal detector settings and a fast scan rate of 60 arcsec s^{-1} over two orthogonal cross-linked scan directions. Here we discuss combined data from two scans per field (the complete survey will comprise eight scans).

PACS data reduction was carried out with the standard pipeline for both the 100- and the 160-μm channels. Dead and saturated pixels were masked. Deglitching was performed in two steps, using the standard multiwavelength median transform deglitcher and another based on sigma-clipping. Bright sources were masked before a high-pass filter was used to reduce $1/f$ noise. Finally, the two orthogonal scans were combined and maps made using the naive map-maker. Overall, the HeViCS PACS data reduction strategy is similar to the approach used for the *Herschel*-ATLAS key programme (Eales et al. 2010), as explained in detail in Ibar et al. (2010). After combining orthogonal scans, the full width at half-maximum (FWHM) beam sizes are approximately 9 and 13 arcsec with pixel sizes of 3.2 and 6.4 arcsec for the 100- and 160-μm channels, respectively.

The SPIRE photometer (Griffin et al. 2010) data were processed up to Level 1 (to the level where the pointed photometer time-lines have been derived) with a custom-driven pipeline script adapted from the official pipeline (*POF5_pipeline.py*, dated 2010 June 8) as provided by the SPIRE Instrument Control Centre (ICC).[1] This JYTHON script was run in the Herschel Interactive Processing Environment (Ott 2010). Our data reduction up to Level 1 is very similar to the Herschel Common Science System/Standard Product Generation v5 with a calibration based on Neptune data.

Specific differences from the standard pipeline were that we used *sigmaKappaDeglitcher* instead of the ICC-default *waveletDeglitcher*. Furthermore, we did not run the default *temperatureDriftCorrection* and the residual, median baseline subtraction. Instead we use a custom method called BriGAdE (Smith et al., in preparation) to remove the temperature drift and bring all bolometers to the same level (equivalent to baseline removal). We have found this method improves the baseline subtraction significantly, especially in cases where there are strong temperature variations during the observation.

Both scans were then combined to make our final maps using the naive mapper provided in the standard pipeline. The FWHMs of the SPIRE beams are 18.1, 25.2 and 36.9 arcsec with pixel sizes of 6, 10 and 14 arcsec at 250, 350 and 500 μm, respectively. The final data products have a mean 1σ noise, determined from the whole of

[1] See 'The SPIRE Analogue Signal Chain and Photometer Detector Data Processing Pipeline' (Griffin et al. 2009 or Dowell et al. 2010) for a more detailed description of the pipeline and a list of the individual modules.

each image, of ∼2.6, 4.5, 0.9, 1.1 and 1.3 mJy pixel^{-1} at 100, 160, 250, 350 and 500 μm, respectively.

To obtain a bright far-infrared selected sample, we carried out our initial object selection at 500 μm. This is because it is the least explored part of the spectrum, it has the lowest resolution, and most galaxies will produce their lowest flux in this band, guaranteeing a detection in all five bands. To produce an objectively selected sample, we used the automatic image detection algorithm SExtractor (Bertin & Arnouts 1996). To minimize background contamination by faint sources, each object was required to have more than 30 connected pixels at $1.5\sigma_{500}$ or above. The result is a 500 μm flux density limit of ∼0.1 Jy for sources with a diameter larger than 1.4 arcmin. Each object was then checked for correspondence with a known Virgo Cluster galaxy. The final sample consists of 78 Virgo Cluster objects, which is 12 per cent of the 629 VCC galaxies in our fields that are listed by GOLDMINE as confirmed cluster members (Gavazzi et al. 2003). Discarded objects are either associated with extended galactic cirrus emission or objects in the background of Virgo. In this paper, our intention is to concentrate on these bright galaxies detected at high S/N. The faintest galaxy in the final sample (see below) being detected with a S/N of ∼15.

Before carrying out aperture photometry on the selected galaxies, the data at other wavelengths were smoothed and re-gridded to the 500-μm resolution and pixel scale. Elliptical apertures were initially chosen by eye using the 500-μm data, with the sky defined by a concentric annulus. These same annuli were then used on the smoothed and re-gridded data at other wavelengths. Independent measurements were carried out on the maps at the original resolution, defining for each galaxy a polygonal aperture that included all pixels with S/N ≥ 2 at 250 μm (the deepest band), and a nearby sky aperture that avoided pixels contaminated by bright background sources. Our results from these two approaches are significantly affected by the apertures chosen and after careful analysis we estimate errors of 17, 10, 8, 8 and 10 per cent at 100, 160, 250, 350 and 500 μm, respectively, due to the choices made.

Independently as part of the HRS data analysis, Ciesla et al. (in preparation) have compared our SPIRE aperture photometry with that derived using apertures set at 1.4 times the galaxy's optical radius and a 60 arcsec width annulus for the background. Mean values of the flux density ratios between these HRS values and those given here are 0.98 ± 0.06, 0.96 ± 0.08 and 0.96 ± 0.09 for 250, 350 and 500 μm, respectively. The scatter between the Ciesla et al. values and those quoted here is 6, 8 and 10 per cent, respectively, that is, very close to the SPIRE aperture uncertainty we estimated above.

As shown in Fig. 1, the four separate 4 × 4 deg^2 fields have a small overlap region. A few of our galaxies fall within these overlap regions and so have been observed independently twice. Also, two of the fields have already been observed with more than two scans. Using the same apertures on these independent measurements leads to an uncertainty in flux values due to noise in the data recording and processing of 20, 10, 2, 3 and 5 per cent at 100, 160, 250, 350 and 500 μm, respectively.

The absolute calibration of the data is thought to be uncertain to 15, 15, 7, 7 and 7 per cent at 100, 160, 250, 350 and 500 μm, respectively (Ibar et al. 2010; Swinyard et al. 2010). Taking the above three uncertainties to be independent, we estimate total uncertainties in our flux values of 30 20, 10, 10 and 15 per cent at 100, 160, 250, 350 and 500 μm, respectively. In Table 1, we list all 78 Virgo bright galaxies with their names, coordinates, velocities, distances and flux values in each band. The coordinates are obtained from centroiding the 500-μm data, and the velocities and distances have been taken from GOLDMINE (Gavazzi et al. 2003). The fluxes in Table 1 do not include colour corrections (see Section 5).

For both PACS and SPIRE data, we can make some comparisons of our results with those obtained by others. Where available (73 galaxies) we have taken *IRAS* 100-μm fluxes from the GOLDMINE data base (Gavazzi et al. 2003) and show their comparison with the PACS in Fig. 2. UGC 7557 stands out as being the only obvious anomalous result, as we measure a barely detected value of 0.13 Jy, while the *IRAS* value is 0.73 Jy. A linear least-squares fit to the data gives the relationship $F(\mathrm{PACS}) = 1.16(\pm0.02)F(IRAS) - 0.69(\pm0.47)$. Using the *ISO*, Tuffs et al. (2002) also measured 100-μm fluxes for 12 of our galaxies (see Fig. 2). The linear least-squares fit to these data gives the relationship $F(\mathrm{PACS}) = 2.52(\pm0.16)F(ISO) - 3.51(\pm1.71)$. This is the least good of our comparison calibrations with an indication that the largest fluxes correspond less well. NGC 4567 has a PACS 100-μm flux a factor of 2.6 larger than that measured by the *ISO* (76.3 compared with 29.3 Jy; Fig. 2), but it is very close to NGC 4568 and will be difficult to separate it from NGC 4568 in the lower resolution *ISO* data. *Spitzer* 160-μm data exist for 44 out of the 78 galaxies in our sample (Bendo, in preparation; see Fig. 3). A linear least-squares fit to the data gives $F(\mathrm{PACS}) = 0.97(\pm0.02)F(\mathrm{MIPS}) + 1.16(\pm0.56)$. There appears to be just a small calibration of-set (PACS fluxes are higher) between the PACS and MIPS. There are 14 galaxies from the ISOPHOT 170-μm Serendipity Survey (Stickel et al. 2004) that are in common with our survey, and we compare these fluxes with ours in Fig. 3. Comparing these 14 galaxies with our 160-μm data, we obtain $F(\mathrm{PACS}) = 0.60(\pm0.05)F(ISO) + 2.4(\pm1.12)$. Here there is a larger discrepancy between the two data sets which appears to be entirely due to NGC 4192 with the *ISO* measurement almost twice that of the PACS (66.6 compared to 37.7 Jy). Removing NGC 4192 from the sample gives $F(\mathrm{PACS}) = 0.94(\pm0.05)F(ISO) + 0.16(\pm0.48)$. There are also 12 galaxies measured at 170 μm in the *ISO* survey of Tuffs et al. (2002) (see Fig. 3). A linear least-squares fit to these data gives $F(\mathrm{PACS}) = 0.93(\pm0.05)F(ISO) + 2.11(\pm1.47)$. Finally, the Planck Consortium have released a point source catalogue of bright sources which, at 350 μm, contains 17 of the galaxies in our list. In Fig. 2, we compare these 350-μm flux densities (we use the flux within an aperture of radius = FWHM) with our SPIRE data, obtaining the relationship $F(\mathrm{SPIRE}) = 0.98(\pm0.05)F(Planck) - 0.37(\pm0.45)$; only NGC 4260 stands out as being an anomaly with regard to the SPIRE and *Planck*.

3 LUMINOSITY FUNCTIONS AND DISTRIBUTIONS

Cosmic dust contributes only a small fraction of the total baryonic mass of galaxies, but although small in mass, it plays a prominent role in how galaxies evolve with time. For example, dust is thought to be the major site for the formation of molecular hydrogen. Radiative cooling by dust grains allows this molecular gas to collapse to form stars and the residual dust is probably a major contributor to the material that forms protoplanetary discs and eventually planets. The link between dust and the formation of stars is confirmed by the close correlation of far-infrared emission at shorter wavelengths (<100 μm) and the star formation rate measured by other means (e.g. Calzetti et al. 2010). Longer wavelength dust emission is probably associated with more extensive colder material distributed throughout galaxies (Bendo et al. 2010, 2011). The comparative

Table 1. The HeViCS Bright Galaxy Sample. Column (1): name; columns (2) and (3): position; column (4): velocity; column (5): distance; and column (6): far-infrared flux density. Note that NGC 4567 and 4568 are very close together and so it is difficult to separate the measurements of one from the other.

(1) Name	(2) RA (J2000)	(3) Dec. (J2000)	(4) v (km s^{-1})	(5) D (Mpc)	(6) F_{500} (Jy)	F_{350} (Jy)	F_{250} (Jy)	F_{160} (Jy)	F_{100} (Jy)
NGC 4165	12:12:12.6	13:14:40.0	1862	32.0	0.15	0.38	0.81	1.19	0.61
IC 00769	12:12:32.6	12:07:22.1	2209	32.0	0.40	0.96	1.81	3.04	0.99
NGC 4189	12:13:47.8	13:25:32.1	2114	32.0	0.99	2.88	6.91	12.26	11.34
NGC 4192	12:13:48.4	14:54:00.5	−139	17.0	5.07	12.87	27.75	37.65	24.24
NGC 4193	12:13:53.7	13:10:22.0	2470	32.0	0.68	1.68	3.51	6.93	2.62
NGC 4197	12:14:38.8	05:48:23.0	2062	32.0	0.67	1.68	3.37	6.37	6.32
IC 03061	12:15:04.6	14:01:42.9	2316	17.0	0.32	0.77	1.56	2.35	1.68
NGC 4206	12:15:17.1	13:01:28.4	704	17.0	1.08	2.20	3.56	4.69	2.35
NGC 4212	12:15:39.0	13:54:08.7	−88	17.0	1.85	5.33	12.96	26.77	21.78
NGC 4216	12:15:54.9	13:08:52.7	139	17.0	3.93	9.99	21.10	31.89	16.47
NGC 4222	12:16:22.5	13:18:20.9	229	17.0	0.86	1.95	3.35	4.19	4.02
NGC 4234	12:17:09.2	03:40:51.1	2031	32.0	0.31	0.93	2.11	4.80	4.73
NGC 4237	12:17:11.5	15:19:26.6	865	17.0	1.01	3.00	7.38	15.16	10.81
NGC 4241	12:17:25.6	06:41:19.6	2239	32.0	0.23	0.59	1.17	1.86	0.44
IC 03115	12:18:00.1	06:39:00.2	732	23.0	0.32	0.62	1.03	1.25	0.38
NGC 4252	12:18:31.6	05:33:53.6	864	32.0	0.12	0.24	0.35	0.55	0.61
NGC 4254	12:18:49.7	14:25:10.8	2404	17.0	8.79	26.29	65.45	130.99	114.25
NGC 4260	12:19:21.2	06:06:03.2	1935	23.0	0.16	0.44	0.88	1.33	0.68
NGC 4266	12:19:42.7	05:32:18.6	1617	32.0	0.17	0.53	1.30	2.63	1.64
NGC 4273	12:19:56.1	05:20:36.3	2379	32.0	1.47	4.20	10.45	24.31	26.01
UGC 7387	12:20:17.8	04:12:04.8	1732	17.0	0.19	0.48	0.94	1.52	0.87
NGC 4289	12:21:02.9	03:43:24.7	2541	17.0	0.48	1.22	2.29	3.14	2.31
NGC 4294	12:21:17.8	11:30:37.8	355	17.0	0.89	2.06	4.16	7.27	5.78
NGC 4298	12:21:33.3	14:36:15.2	1136	17.0	1.66	4.94	11.89	21.95	15.62
NGC 4299	12:21:40.7	11:30:02.6	232	17.0	0.46	1.16	2.41	4.75	4.83
NGC 4302	12:21:42.4	14:35:50.4	1150	17.0	2.89	8.24	18.67	30.44	18.73
NGC 4303	12:21:55.1	04:28:27.8	1566	17.0	8.08	22.55	54.57	114.90	102.95
NGC 4307	12:22:05.7	09:02:29.0	1035	23.0	0.72	2.06	4.58	7.75	4.71
NGC 4309	12:22:12.1	07:08:43.9	1071	23.0	0.22	0.55	1.10	2.03	1.70
NGC 4301	12:22:27.6	04:33:49.3	1278	17.0	0.17	0.45	0.81	1.44	1.52
NGC 4312	12:22:31.3	15:32:19.0	148	17.0	0.55	1.66	4.19	8.62	7.33
NGC 4313	12:22:38.4	11:48:01.5	1442	17.0	0.62	1.81	4.11	8.23	4.73
IC 03225	12:22:38.7	06:40:37.3	2362	23.0	0.20	0.46	0.90	1.40	0.81
NGC 4316	12:22:42.0	09:20:00.0	1250	23.0	0.84	2.16	4.91	9.12	5.92
NGC 4321	12:22:54.9	15:49:24.8	1575	17.0	9.98	28.54	68.31	109.45	76.34
NGC 4324	12:23:06.6	05:15:03.8	1668	17.0	0.36	0.95	1.94	2.71	1.69
NGC 4330	12:23:17.2	11:22:02.0	1563	17.0	0.74	1.80	3.54	5.19	2.42
NGC 4343	12:23:38.3	06:57:20.6	1013	23.0	0.58	1.59	3.60	6.70	5.53
IC 03258	12:23:43.7	12:28:40.7	−430	17.0	0.17	0.40	0.72	1.37	0.80
IC 03259	12:23:47.3	07:11:23.8	1420	23.0	0.22	0.53	1.06	1.37	0.95
NGC 4351	12:24:01.5	12:12:17.4	2316	17.0	0.26	0.68	1.41	2.65	1.41
IC 03268	12:24:07.7	06:36:22.9	727	23.0	0.17	0.41	0.79	1.50	1.77
NGC 4374	12:25:03.7	12:52:55.4	910	17.0	0.13	0.15	0.27	0.86	1.14
NGC 4376	12:25:18.4	05:44:30.1	1138	23.0	0.23	0.54	1.06	2.76	1.60
NGC 4378	12:25:18.5	04:55:23.4	2557	17.0	0.56	1.85	3.36	1.10	1.00
NGC 4380	12:25:22.0	10:01:06.3	963	23.0	0.76	2.23	4.91	6.17	3.04
UGC 7513	12:25:42.8	07:13:01.3	993	23.0	1.02	2.45	4.91	8.35	5.87
NGC 4388	12:25:47.5	12:39:44.7	2515	17.0	1.25	3.50	8.64	20.68	21.41
NGC 4390	12:25:51.5	10:27:33.3	1101	23.0	0.40	0.94	1.89	2.85	1.61
IC 03322	12:25:54.1	07:33:19.5	1202	23.0	0.36	0.91	1.85	2.99	2.67
NGC 4402	12:26:07.4	13:06:44.7	230	17.0	2.08	6.08	14.50	28.15	21.15
UGC7537	12:26:29.6	08:52:19.8	1278	23.0	0.26	0.60	1.11	1.58	0.94
NGC 4413	12:26:32.3	12:36:38.2	103	17.0	0.44	1.16	2.50	4.36	1.94
NGC 4412	12:26:36.5	03:57:55.6	2289	17.0	0.36	1.11	2.77	6.60	6.88
NGC 4416	12:26:46.8	07:55:06.8	1390	17.0	0.40	1.08	2.39	4.79	2.93
UGC 7546	12:26:47.6	08:52:54.2	1272	23.0	0.56	1.24	2.25	2.62	1.08
NGC 4423	12:27:09.8	05:52:56.5	1120	23.0	0.30	0.59	0.99	1.93	1.15
UGC 7557	12:27:10.4	07:15:58.7	932	23.0	0.36	0.73	1.14	0.74	0.13
NGC 4424	12:27:11.3	09:25:14.5	437	23.0	0.32	0.96	2.47	5.52	6.21

Table 1 – *continued*

(1) Name	(2) RA (J2000)	(3) Dec. (J2000)	(4) v (km s^{-1})	(5) D (Mpc)	(6) F_{500} (Jy)	F_{350} (Jy)	F_{250} (Jy)	F_{160} (Jy)	F_{100} (Jy)
NGC 4435	12:27:40.3	13:04:43.9	775	17.0	0.21	0.68	1.87	4.31	4.77
NGC 4438	12:27:44.7	13:00:25.5	104	17.0	1.07	3.23	7.62	15.54	11.40
NGC 4445	12:28:15.9	09:26:10.4	328	23.0	0.20	0.59	1.39	2.44	1.73
NGC 4451	12:28:40.6	09:15:40.7	858	23.0	0.30	0.87	2.21	5.24	4.90
NGC 4459	12:29:00.1	13:58:46.0	1210	17.0	0.19	0.61	1.63	4.26	5.20
NGC 4469	12:29:28.1	08:44:58.7	508	23.0	0.25	0.84	2.05	4.02	3.80
NGC 4466	12:29:29.9	07:41:43.1	759	17.0	0.19	0.40	0.83	1.13	1.10
NGC 4470	12:29:37.9	07:49:26.9	2341	17.0	0.36	1.04	2.44	5.84	5.26
NGC 4486	12:30:49.2	12:23:24.8	1292	17.0	1.28	0.92	0.67	0.92	0.53
NGC 4492	12:30:59.6	08:04:35.2	1777	17.0	0.22	0.65	1.37	2.39	1.07
IC 03476	12:32:40.9	14:02:52.3	−170	17.0	0.43	1.09	2.19	3.34	3.41
NGC 4519	12:33:30.5	08:39:17.6	1216	17.0	1.03	2.47	5.06	9.44	6.48
NGC 4522	12:33:39.7	09:10:32.4	2329	17.0	0.65	1.68	3.56	6.29	5.12
NGC 4526	12:34:03.1	07:41:57.3	448	17.0	0.96	3.02	7.90	17.59	17.33
NGC 4531	12:34:16.0	13:04:32.2	195	17.0	0.22	0.63	1.44	2.59	1.15
NGC 4535	12:34:20.1	08:11:53.5	1964	17.0	5.81	15.63	34.43	49.42	21.89
IC 03521	12:34:39.3	07:09:43.2	593	17.0	0.18	0.60	1.48	2.93	2.36
NGC 4567	12:36:32.4	11:15:27.0	2277	17.0	1.68	5.01	12.64	26.49	20.76
NGC 4568	12:36:33.9	11:14:35.1	2255	17.0	4.12	12.33	30.89	64.45	55.58

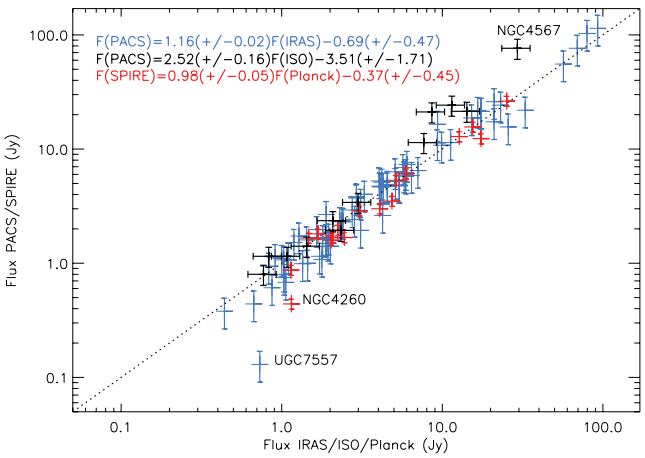

Figure 2. A comparison of *IRAS* (blue) and *ISO* (black) fluxes with the PACS 100-μm fluxes along with the *Planck*/SPIRE 350-μm (red) fluxes. Linear least-squares fit parameters are given at the top left-hand side of the figure. The black dashed line is the one-to-one relationship.

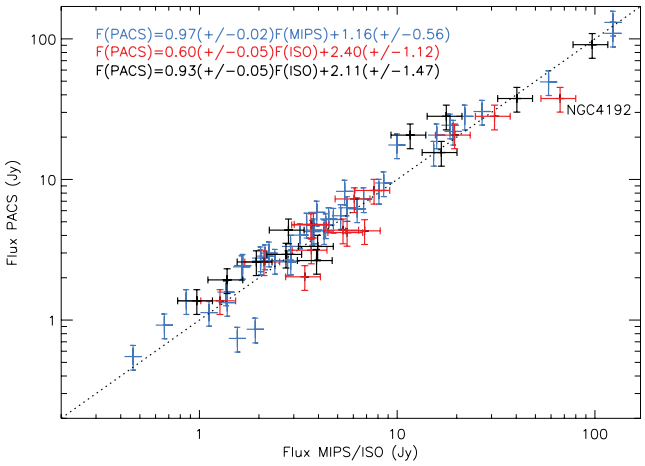

Figure 3. A comparison of the *Spitzer* (MIPS) 160-μm (blue), the Stickel et al. *ISO* 170-μm (red) and the Tuffs et al. *ISO* 170-μm (black) fluxes with the PACS 160-μm fluxes. Linear least-squares fit parameters are given at the top left-hand side of the figure. The black dashed line is the one-to-one relationship.

luminosity of a galaxy at different far-infrared wavelengths is thus a measure of the relative importance of the dust associated with star formation and that which is cold and diffusely distributed throughout the interstellar medium.

The Virgo bright galaxy luminosity function/distributions (total numbers of galaxies within each luminosity interval) for each *Herschel* wavelength are shown in Fig. 4.[2] The shape of these luminosity distributions can be used in comparison with those obtained for galaxies in other environments to assess the influence of that particular environment (field or varying richness of group or cluster) and at different redshifts to assess evolution over cosmic time. Given the proximity of Virgo, and hence the detail and depth of the observations, we expect this bright galaxy sample to act as a benchmark for future studies.

The far-infrared luminosity function/distributions we obtain are quite different from those derived in the optical. At optical wavelengths, large numbers of low-luminosity galaxies are found in the cluster that give rise to a reasonably good Schechter function fit with the faint-end slope of the order of −1.3 to −1.6 (Sabatini et al. 2003). All of our far-infrared luminosity function/distributions turn over at faint luminosities.

All galaxy samples, no matter how selected, are subject to selection effects primarily related to the sensitivity of the observations compared to the surface brightness of the objects. Given that this is an isophotal size selected sample, there may be galaxies that have large enough luminosities to appear in Fig. 4, but are not included in our sample because they are too small at the isophote of choice.

[2] We use the term luminosity function to refer to the 500-μm data because the data are selected at this wavelength. We use the term luminosity distribution for data at other wavelengths.

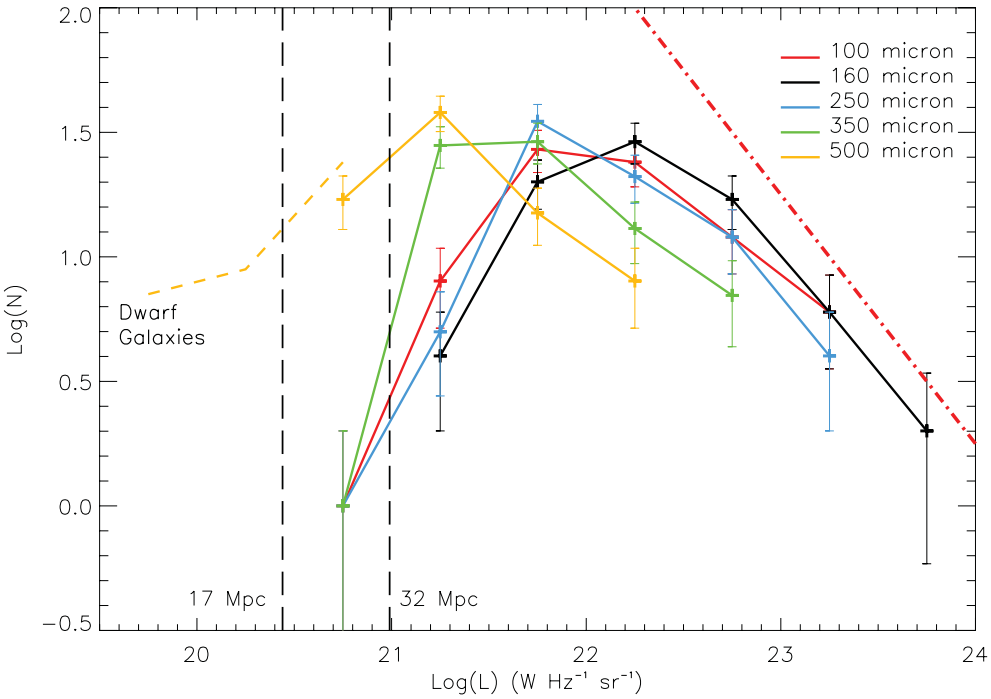

Figure 4. The luminosity distributions derived from the data listed in Table 1. The dot–dashed line indicates a slope of −1 as found by Rowan-Robinson, Helou & Walker (1987) using *IRAS* 100-μm data. The vertical black dashed lines indicate the minimum luminosity at 17 and 32 Mpc for a minimum 500-μm flux density of 0.1 Jy. The yellow dashed line indicates the shape of the 500-μm luminosity distribution, if known star-forming dwarf galaxies, beyond our detection limit, are included.

Future studies will investigate this further, so here we just discuss some relevant issues which indicate that our 500-μm luminosity function and derived luminosity distributions may not be too awry.

(i) Even the lowest luminosity galaxies in the sample are detected at a minimum S/N of 15, that is, the last point of the 500-μm luminosity function is not adversely affected by being close to a limit set by S/N.

(ii) In Davies et al. (2010), we show that the luminosity function/distributions are peaked independent of the wavelength (e.g. 160 μm) used for selection.

(iii) At optical wavelengths, Sandage, Binggeli & Tammann (1985) found that the luminosity distributions of Virgo Cluster bright spiral and elliptical galaxies (analogous to our sample) were Gaussian and only became power laws (Schechter) when the dwarf galaxies were included. These dwarf galaxies are predominantly metal-poor dE galaxies and we have previously shown that these are not detected at 500 μm in our current data (De Looze et al. 2010).

(iv) Confirmed Virgo Cluster galaxies fainter than our 500-μm selection limit have been detected in the HeViCS data, but they are too small to be included in our sample (Grossi et al. 2010). Grossi (private communication) has identified 24 out of 139 late-type dwarf galaxies listed in the VCC that have a measurable 500-μm flux. Six of these lie, according to GOLDMINE, in the most distant structure at 32 Mpc. We have added these 24 galaxies to the 500-μm data shown in Fig. 4 (yellow dashed line) and as can be seen they do not alter our conclusion about a 'peaked' luminosity function.

We have an ongoing programme to try to detect as many VCC galaxies as possible in the HeViCS data. For this programme to seriously change our conclusions, we would need to find a population of far-infrared bright objects that have very low optical luminosities. There is of course always the possibility of far-infrared sources with no optical counterparts, but we would have to show conclusively that they were cluster members and not associated with faint optical sources in the background.

If confirmed, the 'peaked' nature of the far-infrared luminosity function/distributions is similar to the Virgo Cluster H I mass function, where there is also an apparent turnover at low masses (Davies et al. 2004; Taylor 2010). This is also quite different from the low-mass power-law slope of the global H I mass function (Martin et al. 2010; Davies et al. 2011). The straightforward explanation of the different H I mass function shapes is that gas-stripping processes (Doyon & Joseph 1989) in the cluster are more dramatic for low-mass galaxies. Thus, the form of the luminosity function/distributions suggests that this may now also apply to the removal of cosmic dust. Although a number of tidal gas (21-cm) streams (Kent et al. 2007) have been identified in the cluster environment, the identification of intergalactic dust has been a little more controversial and would benefit from additional confirmation (see Stickel et al. 1998, for an example of a detection). The fate of stripped galactic dust is still unclear.

At the current time, the availability of comparison luminosity distributions derived at the wavelengths of interest here is somewhat limited (see Davies et al. 2010). Many of the luminosity distributions derived using *IRAS* data used the 60-μm fluxes as their longest wavelength (see e.g. Soifer et al. 1987; Saunders et al. 1990). With a few exceptions (see Takeuchi et al. 2006, and references therein), the *ISO* also concentrated on shorter wavelengths than those considered here. The same is true of *Spitzer* (Babbedge et al. 2006; Rodighiero et al. 2010).

The most informative comparison is with the *IRAS* 100-μm luminosity function derived by Rowan-Robinson et al. (1987). In a similar way to us, they constructed a far-infrared sample from

Table 2. The mean luminosity and luminosity density in each band for the Virgo Bright Galaxy Sample. The luminosity density using just the galaxies with distances of 17–23 Mpc are given in brackets. The temperatures are those that produce modified blackbody curves that peak in each band ($\beta = 2$).

Band (μm)	Mean luminosity $\times 10^{22}$ (W Hz^{-1} sr^{-1})	Luminosity density $\times 10^{-45}$ (W m^{-3} Hz^{-1})	Temperature (K)
100	3.4 ± 0.6	$6.5(19.7) \pm 0.6$	20.2
160	4.4 ± 0.8	$8.3(25.9) \pm 0.6$	12.6
250	2.4 ± 0.4	$4.6(14.8) \pm 0.2$	8.1
350	1.0 ± 0.2	$1.9(6.3) \pm 0.2$	5.8
500	0.4 ± 0.1	$0.7(2.3) \pm 0.2$	4.0

optically identified galaxies with an available redshift. This is roughly comparable with our Virgo sample in the sense that all the galaxies have to have an optical identification and a distance, but their sample is drawn from a wide range of environments. The Rowan-Robinson et al. luminosity function follows a power-law slope of about -1 from $\sim 10^{24}$ to $\sim 4 \times 10^{21}$ W Hz^{-1} sr^{-1}. Although the luminosity function/distribution normalization is arbitrary when comparing with our data (Fig. 4), it is clear that the Rowan-Robinson et al. luminosity function predicts $\sim 10^3$ more galaxies at the faint end than at the bright end – even with the small numbers in our sample, this is difficult to reconcile with our Virgo data, unless subsequent investigation reveals large numbers of small faint cluster far-infrared sources. The Rowan-Robinson et al. data also include galaxies that are one order of magnitude brighter than the brightest galaxies found in the Virgo Cluster – it has previously been noted that clusters in general do not have the very bright far-infrared sources seen in the field (Bicay & Giovanelli 1987).

Given the apparent shape of the Virgo Cluster luminosity function/distributions, it is currently more informative to simply characterize them by their mean values rather than a poorly fitted and parametrized Schechter function. These mean values are given in Table 2. It is clear that the majority of the far-infrared energy of the cluster is being produced at the shortest of these wavelengths. Using Wien's law for the predicted temperature of a modified blackbody curve with emissitvity β, that is, $T_{\rm d} \approx \frac{14\,142.9}{(5+\beta)\lambda_{\rm max}}$, leads to the temperatures given in Table 2 for each wavelength (band) $\lambda_{\rm max}$ and emissivity $\beta = 2$. Clearly, we expect from this dust temperatures of the order of 13–20 K (see below).

As the luminosity distributions apparently turn over at both the faint and luminous ends, we can make an estimate of the luminosity density in each band. Listed Virgo members in GOLDMINE extend from 17 to 32 Mpc, which is a large distance compared to what is normally assumed for the size of a cluster. So, all densities quoted below will be calculated using both the whole sample and just using those with distances between 23 and 17 Mpc (given in brackets). The volume we sample over 64 deg^2 of sky is ~ 181.3 Mpc^3 for galaxies between 17 and 32 Mpc, and ~ 47.2 Mpc^3 for the reduced sample with distance between 17 and 23 Mpc (68 galaxies). Values for the luminosity density in each band are given in Table 2. It is difficult to make comparisons with previous work because this is a newly explored part of the electromagnetic spectrum. Saunders et al. (1990) using *IRAS* data give a luminosity density of $(4.0 \pm 0.4) \times 10^7$ L$_\odot$ Mpc^{-3} for emission in the range 42.5–122.5 μm from galaxies in all environments. Using this bandpass and our 100-μm luminosity density gives a value of $[1.1(3.3) \pm 0.1] \times 10^9$ L$_\odot$ Mpc^{-3} for this Virgo Cluster sample, a factor of 28(83) higher. At 160 μm, Takeuchi et al. (2006) use *ISO* data to obtain a value of 3.7×10^7 L$_\odot$ Mpc^{-3} again for a sample occupying various environments. Our value for the Virgo Cluster is $[5.1(15.9) \pm 0.6] \times 10^8$ L$_\odot$ Mpc^{-3}, a factor of 14(44) higher. A value of $H_0 = 72$ km s^{-1} Mpc^{-1} has been assumed to adjust the literature luminosity densities.

Simply multiplying the luminosity densities given in Table 2 by the bandwidths (assuming non-overlapping bands, see below), we obtain a Virgo 100–500 μm far-infrared luminosity density of $\rho_{100-500} = [2.2(9.6) \pm 0.3] \times 10^{-32}$ W m^{-3} or $[1.6(7.0) \pm 0.2] \times 10^9$ L$_\odot$ Mpc^{-3} using a solar luminosity of 3.9×10^{26} W.

4 FAR-INFRARED AND OPTICAL LUMINOSITY

The luminosity density ($\rho_{100-500}$) given above was calculated using non-overlapping bands corresponding to each *Herschel* wavelength (not necessarily centred on the nominal wavelength because of the uneven band spacing). This also provides a means of calculating a far-infrared luminosity for each galaxy. We define the *Herschel* far-infrared luminosity as

$$L_{100-500} = 3.1 \times 10^4 d_{\rm Mpc}^2 [(f_{100}\Delta f_{100}) + (f_{160}\Delta f_{160}) + (f_{250}\Delta f_{250}) + (f_{350}\Delta f_{350}) + (f_{500}\Delta f_{500})]\ {\rm L}_\odot,$$

where f_{100}, f_{160}, f_{250}, f_{350} and f_{500}, and $\Delta f_{100} = 18.0$, $\Delta f_{160} = 8.9$, $\Delta f_{250} = 4.6$, $\Delta f_{350} = 3.1$ and $\Delta f_{500} = 1.8$ are the flux density (Jy) and bandwidth (10^{11} Hz) in each band, respectively, and we have again taken the solar luminosity to be 3.9×10^{26} W. For this particular analysis, we prefer this method of calculating the luminosity because it does not depend on any particular fit to the SED, that is, it is valid for galaxies well fitted by a single modified blackbody with any value of emissivity power index (β), those that require two components or more and those that do not have a thermal spectrum.

To check the consistency of our determination of the far-infrared luminosity, we have compared it with that predicted analytically for a galaxy that is well fitted by a modified blackbody (see the next section). For NGC 4254, the analytical value derived from the fit gives $\log(L_{\rm FIR}) = 10.59$, while the above method gives $\log(L_{100-500}) = 10.51$. Far-infrared luminosities ($L_{100-500}$) for each galaxy are listed in Table 3. Comparing the average far-infrared SEDs of the galaxies in the sample, we find the highest flux density (38 per cent) in the 160-μm band.

We can use a similar approach for the apparent stellar luminosity of each galaxy. We define the apparent stellar luminosity as

$$L_{0.4-2.5} = 3.1 \times 10^7 d_{\rm Mpc}^2 [(f_g\Delta f_g) + (f_r\Delta f_r) + (f_i\Delta f_i) + (f_J\Delta f_J) + (f_H\Delta f_H + (f_K\Delta f_K))]\ {\rm L}_\odot,$$

Table 3. Colour corrections for a $\beta = 2$ modified blackbody of temperature T. Pipeline fluxes (i.e. calibrated assuming $\nu F_\nu =$ constant) should be multiplied by the above factors to retrieve the corrected fluxes. For the SPIRE bands, the values without brackets are for extended sources, while those within brackets are for point sources.

T (K)	100 μm	160 μm	250 μm	350 μm	500 μm
15	0.96	1.06	1.00 (0.98)	0.99 (0.96)	0.99 (0.92)
20	1.03	1.03	0.99 (0.96)	0.98 (0.94)	0.98 (0.90)
25	1.03	0.99	0.08 (0.94)	0.97 (0.93)	0.97 (0.88)

where f_g, f_r, f_i, f_J, f_H and f_K, and $\Delta f_g = 1.9$, $\Delta f_r = 1.1$, $\Delta f_i = 1.6$, $\Delta f_J = 0.9$, $\Delta f_H = 0.3$ and $\Delta f_K = 0.5$ are the flux (Jy) and bandwidth (10^{14} Hz) in each band, respectively. The g-, r- and i-band data ($\lambda_g = 0.48\,\mu$m, $\lambda_r = 0.62\,\mu$m, $\lambda_i = 0.76\,\mu$m) are taken from the Sloan Digital Sky Survey (SDSS). Automated magnitude derivations from within the SDSS data base are notoriously inaccurate for extended sources, so for 54 sources where the data are available we have used SDSS magnitudes derived from our own surface photometry as described in Cortese et al. (2011). For the additional 24 galaxies, we have used SDSS data from the NASA Extragalactic Database (NED). For most of these galaxies, the magnitudes are plausibly consistent with those given in the near-infrared. For two galaxies (UGC 7557 and NGC 4451), there are no consistent SDSS magnitudes and we have set their apparent luminosities in these bands to zero. As we will see below, this does not greatly affect our calculations because by far the largest fraction of the apparent stellar luminosity is emitted in the near-infrared. The SDSS AB magnitudes are converted to Jy using a zero-point of $K_{\rm SDSS} = 8.9$. In the near-infrared, we have used the 2MASS which lists J-, H- and K-band (total) magnitudes for all of our galaxies ($\lambda_J = 1.25\,\mu$m, $\lambda_H = 1.65\,\mu$m, $\lambda_K = 2.17\,\mu$m). The 2MASS website gives the following zero-points for the conversion of magnitudes to Jy: $K_J = 8.01$, $K_H = 7.53$, $K_K = 7.06$.

Considering the average SED of all the galaxies in the sample, but this time in the optical, the highest flux density is produced in the H band (28 per cent of the total), while in the J and K bands it is 23 and 22 per cent, respectively, thus justifying our statement made above that by far the largest fraction of the escaping starlight is emitted in the near-infrared bands.

Summing the contribution from all the galaxies leads to an optical luminosity density of $\rho_{0.4-2.5} = 5.0(20.0) \times 10^9\ {\rm L}_\odot\ {\rm Mpc}^{-3}$, some 3.1(2.9) times larger than the far-infrared value given in the previous section. For their *ISO* sample of Virgo galaxies, Popescu et al. (2002) obtain values of 5.7 and 2.3 for the ratio of optical to far-infrared luminosity in early- and late-type galaxies, respectively, consistent with our global value. There are of course some very optically luminous galaxies like NGC 4486 (M87) and NGC 4374 (M84) that emit little in the far-infrared. The range of both optical and far-infrared luminosities for the galaxies in this sample is shown in Fig. 5.

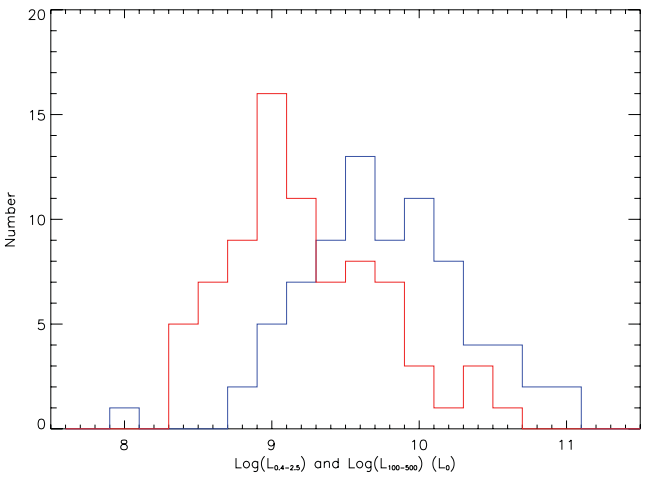

Figure 5. A comparison of the range of optical luminosity in solar units from 0.4 to 2.5 μm (blue) with that in the far-infrared from 100 to 500 μm (red).

We can use the optical and far-infrared luminosities to make a crude estimate of the 'typical' optical depth ($\langle\tau\rangle$) experienced by a photon as it leaves a galaxy, based on a simple screen of dust model:

$$\langle\tau\rangle = \ln\left(1.0 + \frac{L_{100-500}}{L_{0.4-2.5}}\right).$$

Values of $\langle\tau\rangle$ are also listed in Table 4. The mean value for galaxies in this sample is $\langle\tau\rangle_{\rm mean} = 0.4 \pm 0.1$, so on average the optical energy emerging from regions of intermediate optical depth is neither totally optically thin nor totally optically thick. This mean value may be high when compared to galaxies in general because this is a far-infrared-selected sample. Values of $\langle\tau\rangle$ range from 0.04 to 2.76. The two 'optically-thick' galaxies with $\langle\tau\rangle$ greater than unity are both late-type spirals – NGC 4234 (Sc) and NGC 4299 (Scd). As galactic dust is typically confined to a relatively thin disc, the value of τ should be dependent on the inclination of each galaxy to the line of sight. It is therefore surprising that both NGC 4234 and 4299 are relatively face-on galaxies with inclinations of approximately 40° and 20°, respectively. In the optical, both galaxies show signs of possible disturbance and so maybe the dust has been 'stirred up' in these two galaxies. Given the complexities of the relative distributions of stars and dust, a full understanding of the radiative processes that give rise to dust emission will only come about by carrying out detailed radiative transfer modelling (e.g. Bianchi, Davies & Alton 2000a; Baes & Dejonghe 2001; Bianchi 2008). The above value of $\langle\tau\rangle_{\rm mean}$ is very close to the value given in Saunders et al. (1990), derived in a similar way using *IRAS* data ($\langle\tau\rangle^{IRAS}_{\rm mean} = 0.3 \pm 0.1$). The value we find implies that on average 33 ± 7 per cent of the stellar radiation of a galaxy is absorbed by dust. The value is in agreement with that found by Popescu & Tuffs (2002) using a sample of late-type Virgo galaxies observed with the *ISO*. After removing a contribution of hotter dust using data at 60 μm, they fitted the 100- and 170-μm fluxes with a single-temperature modified blackbody with $\beta = 2$ and extrapolated to longer wavelength. Using the *Herschel* data up to 500 μm, we will show in the next section that indeed this simple model can describe very well the dusty thermal SED in most of our sample.

5 DUST, GAS AND STELLAR MASS

In order to derive the dust temperature and masses, we fitted the SED for each galaxy, as defined by the *Herschel* flux densities in Table 1, with a single-temperature modified blackbody. We followed the same procedure as adopted in Smith et al. (2010), Bendo et al. (2010) and Magrini et al. (2011) (see the later work for a discussion of the uncertainties when using a single-temperature model).

We adopted a power-law dust emissivity $\kappa_\lambda = \kappa_0(\lambda_0/\lambda)^\beta$, with spectral index $\beta = 2$ and emissivity $\kappa_0 = 0.192\,{\rm m}^2\ {\rm kg}^{-1}$ at $\lambda_0 = 350\,\mu$m. These values reproduce the behaviour of models of Milky Way dust in the far-infrared–submillimetre, which were also found to reproduce the dust emission SED in several other galaxies (Draine 2003; Draine et al. 2007). The fit was obtained with a standard χ^2 minimization technique. The monocromatic flux densities measured from the images, and reported in Table 1, come from the pipeline calibration. They have been derived from the passband-weighted flux density (measured by the instruments), applying a colour correction for a flat energy spectrum ($F_\nu \propto \nu^{-1}$). We retrieved the passband-weighted flux density by removing this correction (for the SPIRE, this is equivalent to dividing the pipeline flux densities by the K_4 factor for point sources; SPIRE Observers' Manual 2010) and then fitted to the data the average of the model over the spectral response function for each of the bands. We used the

Table 4. The Herschel Virgo Cluster Survey Bright Galaxy Sample. Column (1): name; column (2): absolute B magnitude; column (3): stellar mass; column (4): H I mass; column (5): dust mass; column (6): dust temperature; column (7): stellar luminosity from 0.4 to 2.5 μm; column (8): far-infrared luminosity from 100 to 500 μm; column (9): mean optical depth; column (10): stellar-to-atomic gas mass ratio; and column (11): atomic gas-to-dust mass ratio. The B-, V- and H-band magnitudes, used to calculate stellar mass, are taken from the GOLDMINE data base. The mean fractional dust mass and temperature errors are approximately 19 and 6 per cent, respectively. Seven galaxies have no detected atomic hydrogen. Two galaxies have no dust mass and temperatures listed because their SEDs are not well fitted by a thermal spectrum. Stellar luminosities were calculated using SDSS and 2MASS data. Far-infrared luminosities were calculated using the data from this paper.

(1) Name	(2) M_B	(3) $\log(M_{\rm stars})$ ($M_\odot$)	(4) $\log(M_{\rm H\,I})$ ($M_\odot$)	(5) $\log(M_{\rm Dust})$ ($M_\odot$)	(6) $T_{\rm d}$ (K)	(7) $\log(L_{0.4-2.5})$ ($L_\odot$)	(8) $\log(L_{100-500})$ ($L_\odot$)	(9) $\langle\tau\rangle$	(10) $M_{\rm stars}/M_{\rm H\,I}$	(11) $M_{\rm H\,I}/M_{\rm Dust}$
NGC 4165	−17.99	9.77	8.39	6.97 ± 0.07	18.2 ± 0.9	9.67	8.93	0.17	24.0	26.3
IC 00769	−19.13	9.98	9.48	7.44 ± 0.07	17.0 ± 0.8	9.71	9.26	0.30	3.2	109.6
NGC 4189	−19.84	10.39	9.40	7.65 ± 0.07	21.8 ± 1.3	10.08	10.05	0.66	9.8	56.2
NGC 4192	−20.42	10.88	9.63	7.93 ± 0.07	18.4 ± 0.9	10.56	9.93	0.21	17.8	50.1
NGC 4193	−19.24	10.29	9.24	7.60 ± 0.07	18.4 ± 0.9	10.11	9.62	0.28	11.2	43.7
NGC 4197	−19.15	9.91	9.71	7.46 ± 0.08	20.6 ± 1.3	9.80	9.79	0.68	1.6	177.8
IC 03061	−16.77	9.23	8.79	6.69 ± 0.08	18.7 ± 1.0	9.08	8.74	0.37	2.8	125.9
NGC 4206	−18.15	9.72	9.38	7.31 ± 0.08	16.1 ± 0.8	9.63	8.99	0.21	2.2	117.5
NGC 4212	−19.33	10.27	8.91	7.35 ± 0.07	22.4 ± 1.3	10.04	9.80	0.45	22.9	36.3
NGC 4216	−20.31	10.94	9.25	7.83 ± 0.07	18.3 ± 0.9	10.66	9.81	0.13	49.0	26.3
NGC 4222	−17.20	9.57	9.03	7.20 ± 0.09	16.8 ± 1.0	9.25	9.07	0.51	3.5	67.6
NGC 4234	−19.05	9.61	8.88	7.08 ± 0.08	23.3 ± 1.5	9.36	9.65	1.09	5.4	63.1
NGC 4237	−18.49	10.01	8.32	7.11 ± 0.07	22.0 ± 1.2	9.89	9.53	0.36	49.0	16.2
NGC 4241	−19.55	10.28	8.45	7.28 ± 0.06	16.3 ± 0.6	10.21	9.01	0.06	67.6	14.8
IC 03115	−17.96	9.35	9.03	7.11 ± 0.07	15.1 ± 0.6	9.14	8.62	0.26	2.1	83.2
NGC 4252	−17.74	9.25	9.00	6.88 ± 0.11	16.0 ± 1.1	9.26	8.77	0.28	1.8	131.8
NGC 4254	−20.70	10.67	9.65	8.02 ± 0.07	22.7 ± 1.3	10.59	10.51	0.60	10.5	42.7
NGC 4260	−19.22	10.38	–	6.73 ± 0.07	18.2 ± 0.9	10.09	8.69	0.04	–	–
NGC 4266	−19.04	10.24	–	6.93 ± 0.07	21.5 ± 1.1	9.81	9.29	0.26	–	–
NGC 4273	−20.04	10.33	9.54	7.71 ± 0.08	24.4 ± 1.6	10.19	10.38	0.93	6.2	67.6
UGC 7387	−16.11	9.05	8.39	6.49 ± 0.07	18.5 ± 0.9	8.96	8.50	0.30	4.6	79.4
NGC 4289	−16.56	9.52	9.02	6.92 ± 0.08	17.9 ± 0.9	9.25	8.88	0.35	3.2	125.9
NGC 4294	−18.47	9.59	9.22	7.06 ± 0.08	19.5 ± 1.1	9.59	9.24	0.37	2.3	144.5
NGC 4298	−19.20	10.12	8.94	7.36 ± 0.07	21.3 ± 1.1	10.00	9.69	0.40	15.1	38.0
NGC 4299	−18.16	8.98	9.04	6.72 ± 0.08	21.2 ± 1.4	7.94	9.11	2.76	0.9	208.9
NGC 4302	−18.84	10.32	9.24	7.66 ± 0.07	19.7 ± 1.0	10.08	9.81	0.43	12.0	38.0
NGC 4303	−20.85	10.71	9.68	7.96 ± 0.08	22.7 ± 1.4	10.66	10.46	0.49	10.7	52.5
NGC 4307	−19.03	10.12	8.15	7.31 ± 0.07	19.8 ± 1.0	10.09	9.48	0.22	93.3	6.9
NGC 4309	−18.01	9.80	7.64	6.72 ± 0.08	20.1 ± 1.2	9.65	8.96	0.19	144.5	8.3
NGC 4301	−17.51	8.99	9.08	6.37 ± 0.09	19.6 ± 1.3	9.09	8.61	0.28	0.8	512.9
NGC 4312	−18.69	9.94	8.08	6.82 ± 0.07	22.9 ± 1.4	9.85	9.32	0.26	72.4	18.2
NGC 4313	−18.65	10.12	8.02	6.96 ± 0.07	20.6 ± 1.1	9.93	9.22	0.18	125.9	11.5
IC 03225	−17.32	9.16	8.81	6.76 ± 0.08	18.1 ± 0.9	9.02	9.06	0.74	2.2	134.9
NGC 4316	−18.12	10.03	9.01	7.32 ± 0.00	20.3 ± 0.0	9.81	9.55	0.44	10.5	49.0
NGC 4321	−21.13	10.90	9.44	8.17 ± 0.07	20.3 ± 1.0	10.77	10.39	0.35	28.8	18.6
NGC 4324	−18.58	10.15	8.73	6.80 ± 0.07	18.3 ± 0.9	9.94	8.78	0.07	26.3	85.1
NGC 4330	−18.01	9.71	8.61	7.13 ± 0.07	17.5 ± 0.8	9.55	9.01	0.25	12.6	30.2
NGC 4343	−18.61	10.16	8.78	7.13 ± 0.08	21.2 ± 1.2	9.96	9.47	0.28	24.0	44.7
IC 03258	−17.31	8.95	8.45	6.39 ± 0.08	18.6 ± 1.0	7.49	8.45	2.32	3.2	114.8
IC 03259	−17.45	9.40	8.40	6.84 ± 0.08	17.9 ± 0.9	9.23	8.77	0.30	10.0	33.1
NGC 4351	−18.16	9.29	8.52	6.60 ± 0.07	19.3 ± 1.0	9.40	8.72	0.19	5.9	83.2
IC 03268	−18.01	9.27	8.89	6.56 ± 0.09	20.4 ± 1.4	9.35	8.92	0.31	2.4	213.8
NGC 4374	−20.97	10.99	8.96	–	–	10.90	8.43	–	107.2	–
NGC 4376	−17.98	9.35	8.83	6.69 ± 0.08	20.5 ± 1.2	9.32	9.00	0.39	3.3	138.0
NGC 4378	−18.63	10.16	8.84	–	–	9.96	8.65	0.05	20.9	–
NGC 4380	−19.38	10.40	8.47	7.45 ± 0.07	18.0 ± 0.8	10.25	9.36	0.12	85.1	10.5
UGC 7513	−18.04	9.91	9.45	7.42 ± 0.08	19.2 ± 1.1	9.66	9.54	0.57	2.9	107.2
NGC 4388	−19.28	10.24	8.65	7.08 ± 0.08	24.4 ± 1.6	10.14	9.75	0.34	38.9	37.2
NGC 4390	−18.39	9.51	8.90	7.08 ± 0.07	18.1 ± 0.9	9.58	9.04	0.25	4.1	66.1
IC 03322	−17.58	9.57	8.71	6.96 ± 0.08	19.6 ± 1.1	9.44	9.15	0.42	7.2	56.2
NGC 4402	−18.51	10.11	8.66	7.43 ± 0.07	21.6 ± 1.2	9.90	9.81	0.60	28.2	17.0
UGC 7537	−18.17	9.36	9.23	6.91 ± 0.08	17.5 ± 0.9	9.15	8.80	0.37	1.3	208.9
NGC 4413	−18.21	9.60	8.29	6.87 ± 0.07	18.7 ± 0.9	9.59	8.90	0.19	20.4	26.3
NGC 4412	−18.06	9.59	8.33	6.56 ± 0.08	24.8 ± 1.6	9.51	9.25	0.44	18.2	58.9
NGC 4416	−17.89	9.50	8.41	6.74 ± 0.07	20.5 ± 1.1	9.36	9.00	0.36	12.3	46.8

Table 4 – *continued*

(1) Name	(2) M_B	(3) $\log(M_{\rm stars})$ ($M_\odot$)	(4) $\log(M_{\rm H\,I})$ ($M_\odot$)	(5) $\log(M_{\rm Dust})$ ($M_\odot$)	(6) $T_{\rm d}$ (K)	(7) $\log(L_{0.4-2.5})$ ($L_\odot$)	(8) $\log(L_{100-500})$ ($L_\odot$)	(9) $\langle\tau\rangle$	(10) $M_{\rm stars}/M_{\rm H\,I}$	(11) $M_{\rm H\,I}/M_{\rm Dust}$
UGC 7546	−18.75	9.57	9.34	7.34 ± 0.07	16.0 ± 0.7	9.60	8.98	0.22	1.7	100.0
NGC 4423	−17.92	9.23	9.20	6.85 ± 0.09	18.0 ± 1.1	9.39	8.87	0.26	1.1	223.9
UGC 7557	−18.54	9.24	9.43	7.42 ± 0.07	12.8 ± 0.4	8.83	8.45	0.35	0.6	102.3
NGC 4424	−19.48	10.18	8.59	6.77 ± 0.07	24.8 ± 1.5	10.12	9.46	0.20	38.9	66.1
NGC 4435	−19.35	10.44	–	6.32 ± 0.08	25.9 ± 1.7	10.33	9.08	0.06	–	–
NGC 4438	−20.03	10.70	8.68	7.14 ± 0.02	21.9 ± 0.3	10.27	9.54	0.17	104.7	34.7
NGC 4445	−18.12	9.86	8.06	6.72 ± 0.07	20.8 ± 1.1	9.69	9.00	0.19	63.1	21.9
NGC 4451	−18.37	9.79	8.50	6.75 ± 0.08	24.2 ± 1.5	9.34	9.39	0.75	19.5	56.2
NGC 4459	−19.63	10.60	–	6.22 ± 0.08	27.2 ± 2.0	10.45	9.10	0.04	–	–
NGC 4469	−19.62	10.57	–	6.75 ± 0.07	23.2 ± 1.4	10.38	9.28	0.08	–	–
NGC 4466	−16.55	8.98	8.16	6.43 ± 0.08	18.4 ± 1.1	8.86	8.50	0.36	6.6	53.7
NGC 4470	−17.97	9.43	8.63	6.58 ± 0.08	23.5 ± 1.5	9.44	9.16	0.42	6.3	112.2
NGC 4486	−21.32	11.13	–	–	–	11.05	8.37	–	–	–
NGC 4492	−18.02	9.79	7.94	6.60 ± 0.07	18.8 ± 0.9	9.81	8.64	0.07	70.8	21.9
IC 03476	−17.80	9.18	8.39	6.79 ± 0.08	19.4 ± 1.2	9.07	8.97	0.59	6.2	39.8
NGC 4519	−18.69	9.63	9.43	7.14 ± 0.08	19.7 ± 1.1	9.65	9.32	0.39	1.6	195.0
NGC 4522	−18.18	9.57	8.63	6.94 ± 0.08	20.2 ± 1.2	9.53	9.18	0.37	8.7	49.0
NGC 4526	−20.35	10.95	9.33	7.01 ± 0.07	24.5 ± 1.5	10.72	9.66	0.08	41.7	208.9
NGC 4531	−18.68	9.99	–	6.57 ± 0.07	19.2 ± 0.9	9.77	8.67	0.08	–	–
NGC 4535	−20.42	10.63	9.59	8.04 ± 0.07	18.0 ± 0.8	10.48	9.97	0.27	11.0	35.5
IC 03521	−17.23	9.27	7.94	6.37 ± 0.07	22.7 ± 1.3	9.17	8.84	0.39	21.4	37.2
NGC 4567	−19.24	10.01	8.69	7.31 ± 0.07	22.7 ± 1.3	10.01	9.79	0.47	20.9	24.0
NGC 4568	−19.93	10.49	8.99	7.68 ± 0.07	23.0 ± 1.4	10.25	10.20	0.63	31.6	20.4

appropriate response functions for the PACS and SPIRE bands. The above procedure is equivalent to applying colour corrections to the pipeline monochromatic fluxes, if a SED model is known a priori. The colour corrections are given in Table 3. Given the nature of most of our sources, we used the SPIRE spectral response functions for extended emission. Since these corrections are much smaller than the assumed errors in each band, the fluxes given in Table 1 have not been colour corrected. In a few of our galaxies, the SPIRE fluxes might be dominated by point source emission and thus need a larger colour correction (see Table 3). Even in this case, the colour corrections are of the order of or less than the errors derived above.

Remarkably, plotting the data given in Table 1 shows that the majority of galaxies are well fitted by this single-temperature (modified) blackbody curve with fixed emissivity index; the fits are illustrated in Fig. 6 (ordered by χ^2 value). There are three notable exceptions to this. The early-type galaxies NGC 4486 (M87) and NGC 4374 (M84) show departures from a thermal spectrum (Boselli et al. 2010), particularly at longer wavelengths. As discussed in Baes et al. (2010), specifically for NGC 4486, both these galaxies require modelling of the synchrotron component and its removal before the thermal dust spectrum can be analysed. The third galaxy, NGC 4378, is an early-type spiral with a Seyfert nucleus. Its SED does not appear to be contaminated by a non-thermal contribution, but rather dominated by a colder dust component, because its 160-μm flux is lower than expected when compared to the other values. NGC 4378 requires more detailed radiative transfer modelling and probably a multicomponent dust model before a substantial cold dust component is confirmed. Further modelling of these galaxies with peculiar SEDs is deferred to future papers. Here we concentrate on dust emission and those galaxies that can be fitted by a thermal spectrum.

A few galaxies do not fit a thermal spectrum as well as others, though they do not show any clear evidence of a non-thermal component. For example, NGC 4423 and 4252 have a reduced chi-squared of $\chi^2 > 2$, and NGC 4241, 4301, 4206, 4466, 4376, 4222 and IC 3268 have $1 < \chi^2 < 2$ where χ^2 is derived from the best model fit to the data. We nevertheless use the best single-temperature fitting parameters for these galaxies and defer more complicated fits to later papers.

Derived dust masses and temperatures (75 galaxies) within these 500-μm determined apertures are in the range $10^{6.22}$–$10^{8.17}$ $M_\odot$ and 12.8–27.2 K, with mean values of $10^{7.31}$ $M_\odot$ and 20.0 K, respectively (Table 4). This illustrates the potential sensitivity of the full-depth survey to low dust masses ($<10^6$ $M_\odot$) and the existence of a significant cold dust component ($T < 20$ K). Prior to the availability of observations at wavelengths longer than about 100 μm, calculated galaxy dust masses and temperatures from surveys similar to the HeViCS were typically $10^{6.6}$ $M_\odot$ and 30–50 K, respectively (taken from Soifer et al. 1987 where they have 31 galaxies in common with the HeViCS, see also Devereux & Young 1990). The typical dust mass is now almost an order of magnitude higher and the temperature almost 20 K colder (see also Tuffs et al. 2002).

Interestingly, the coldest galaxy in the sample (12.8 K) is UGC 7557, the galaxy with the most discrepant *IRAS* 100-μm flux (Fig. 6). It is barely detected in the PACS 100-μm data, but is relatively strongly detected in the other bands. The data provide a reasonably good fit to a modified blackbody curve with a calculated dust mass of $10^{7.42}$ $M_\odot$. UGC 7557 is classified as an Scd galaxy and appears to be of rather low surface brightness in the optical. Compared to the other galaxies in this sample, it is also little underluminous in the optical with a B-band absolute magnitude of −18.5. If it is very cold dust, then its origin is unclear; being apparently of low surface brightness, the dust may just be farther away from the stars. Alternately, the dust in this low-luminosity galaxy may have a different emissivity and/or size distribution. We will be investigating this further, once the full-depth HeViCS data become available. The complete distribution of dust temperatures is shown in Fig. 7.

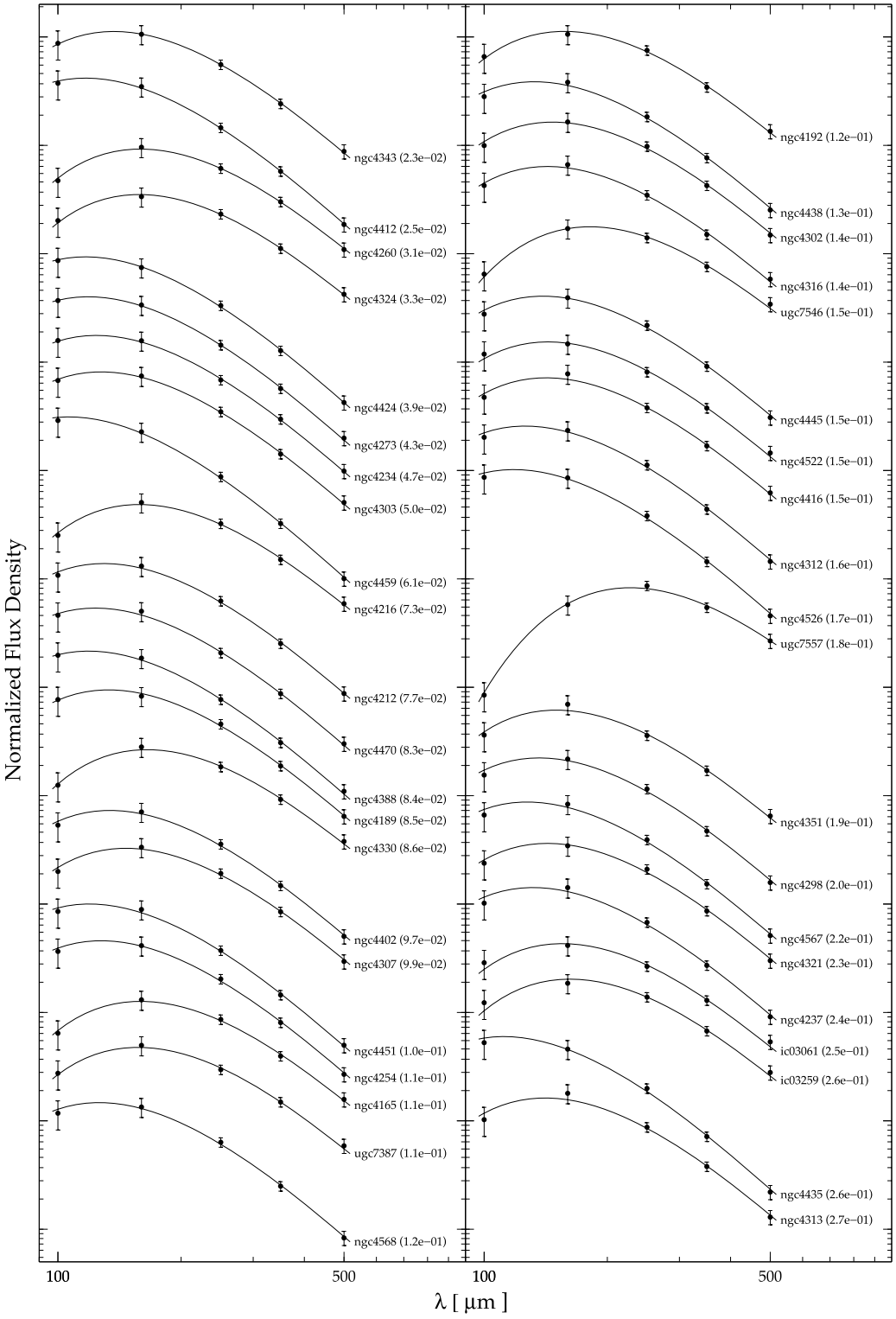

Figure 6. The SEDs of the Bright Galaxy Sample and modified blackbody fits ordered by reduced χ^2 value (given in parentheses). Three galaxies that are not well fitted by a modified blackbody are shown by the dashed line.

We have calculated the stellar masses ($M_{\rm star}$) for each galaxy (Table 4) using the prescription given in Bell et al. (2003), that is,

$$\log M_{\rm star} = -0.359 + 0.21(B-V) + \log \frac{L_H}{\rm L_\odot}.$$

L_H has been calculated using an H-band absolute magnitude for the Sun of $\rm M_H^\odot = 3.32$, and $(B-V)$ values have been taken from the GOLDMINE data base (Gavazzi et al. 2003).

Where available (71 out of the 78 galaxies), we have also taken atomic hydrogen gas masses ($M_{\rm H\,I}$) for each galaxy from the GOLDMINE data base; these are also given in Table 4 along with the dust

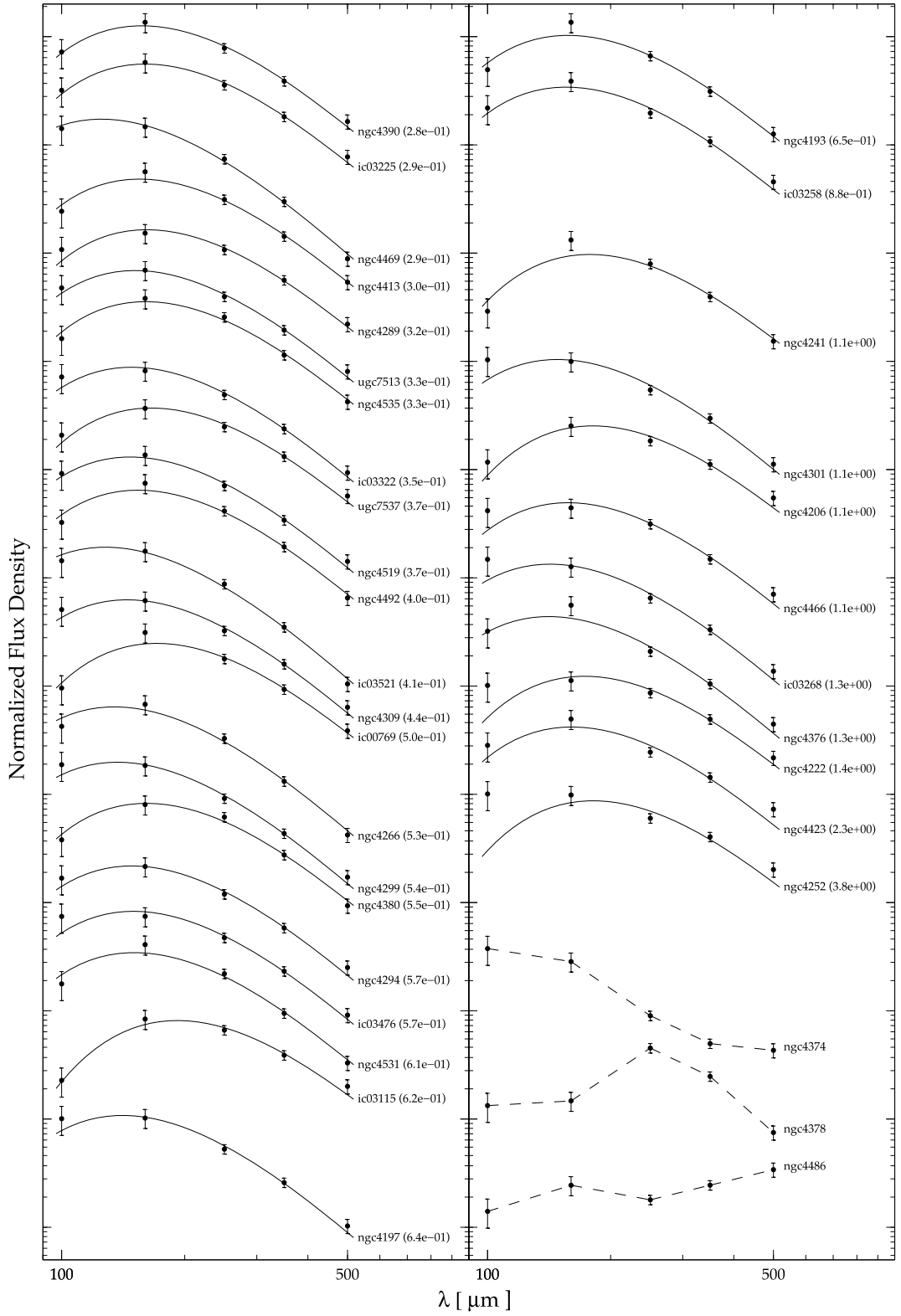

Figure 6 – *continued*

masses. In Fig. 8, we show the distribution of mass in each of the three components, dust, gas and stars. In Fig. 9, we show the mass ratio of stars to atomic gas and atomic gas to dust; these have mean values of 15.1 and 58.2, respectively. We suggest that a factor of ∼2.9 (see below) can be used to convert atomic gas to total gas ($H\,I + H_2$) in which case the mean values of the mass ratios are ∼5 and ∼170, respectively. The local value of the gas-to-dust ratio for the Milky Way is ∼143 (Draine et al. 2007).

By very simply dividing the total mass in each component by the volume sampled [∼181.1(47.2) Mpc^3], we can calculate the cluster

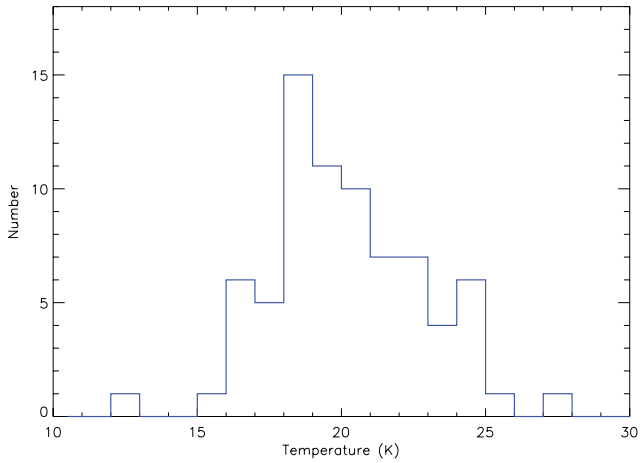

Figure 7. The distribution of dust temperature.

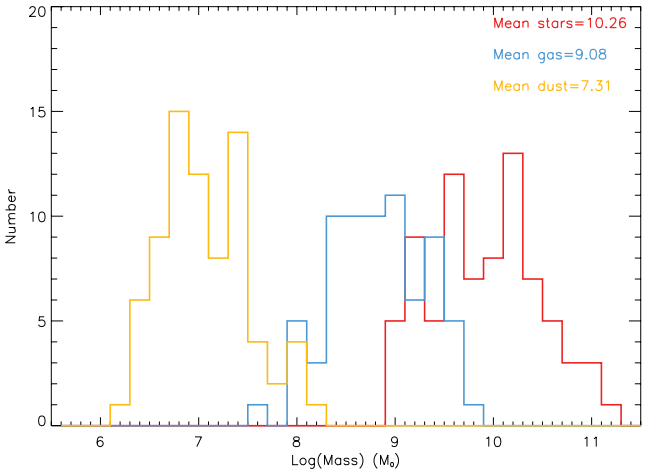

Figure 8. The distribution of stellar mass, atomic gas mass and dust mass. All 78 galaxies have measured stellar masses, 71 have measured atomic gas masses and 76 have measured dust masses.

mass densities. Provided the luminosity distributions in each far-infrared band are peaked, the total cluster dust mass should be well constrained by our sample galaxies, unless there is a significant dust component in the intergalactic medium (Stickel et al. 1998). From the dust in our sample galaxies, we derive a cluster dust mass density of $[8.6(27.8) \pm 1.6] \times 10^6$ $M_\odot$ Mpc^{-3}. This compares with a recent determination of the local dust mass density for galaxies in all environments of $(2.2 \pm 0.4) \times 10^5$ $M_\odot$ Mpc^{-3} (Dunne et al. 2011), that is, the Virgo Cluster is overdense in dust by about a factor of 39(126). The Virgo Cluster H I mass function is also peaked (Davies et al. 2004; Taylor 2010), so again the H I gas in these galaxies should provide a good estimate of the cluster total. From our sample of 71 galaxies, we derive an H I mass density of $4.6(13.9) \times 10^8$ $M_\odot$ Mpc^{-3}. The error on this is uncertain because the H I masses come from a wide variety of sources. Recently, Davies et al. (2011) measured a local 'field' H I mass density of $(7.9 \pm 1.2) \times 10^7$ $M_\odot$ Mpc^{-3} (see also Martin et al. 2010). Thus, the Virgo Cluster is overdense in H I by a factor of only about 6(18). Using the Davies et al. and Dunne et al. values for the global H I and dust mass densities gives a local 'field' atomic gas-to-dust ratio of 359, while the same ratio in the cluster is only 54(50) (total atomic gas mass divided by total dust mass). At face value, these relative overdensities in dust and gas indicate that the cluster galaxies have

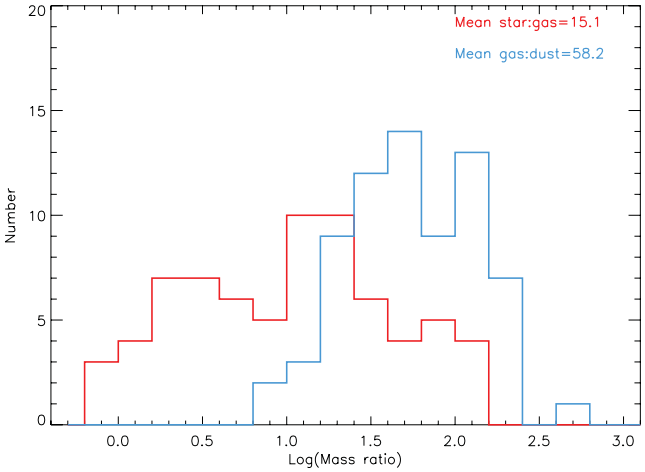

Figure 9. The star-to-atomic gas mass ratio (red) and atomic gas-to-dust mass ratio (blue). Numbers quoted are the mean of the individual values for each galaxy.

either processed more gas through stars, and hence created more metals, or they have lost gas and not dust when compared to the general population of galaxies. H I complexes within the cluster, but external to previously identified galaxies, have been found by Kent et al. (2007), but they only represent a small fraction of the cluster atomic gas.

Comparing stellar mass functions is not quite so straightforward because of uncertainties in the faint-end slope of the Virgo Cluster luminosity distribution, that is, the numbers of faint dwarf galaxies (see Sabatini et al. 2003, and references therein). We obtain from the stars in our sample galaxies a value of $7.8(29.7) \times 10^9$ $M_\odot$ Mpc^{-3} for the stellar density. Baldry, Glazebrook & Driver (2008) recently derived the local galaxy stellar mass function and from it a stellar mass density of $(2.3 \pm 1.2) \times 10^8$ $M_\odot$ Mpc^{-3}. This is 34(129) times smaller than our value for Virgo. Interestingly, the stars and dust are in rough agreement as to the value of the overdensity that Virgo represents, while the atomic gas does not concur. Where required in the above derivations, we have used $H_0 = 72\,\mathrm{km\,s^{-1}}$, $\Omega_\mathrm{m} = 0.27$, $\Omega_\Lambda = 0.73$.

6 CONCLUSIONS

The HeViCS is providing unprecedented high-resolution data, at far-infrared wavelengths, on some of the largest angular sized galaxies in the sky. In this paper, we have described some of the global properties of these galaxies. The Virgo bright galaxy sample discussed here consists of 78 galaxies selected at 500 μm each with a confirmed Virgo Cluster optical counterpart. Each galaxy is detected in each of the five (100–500 μm) far-infrared bands. We have carried out aperture photometry on each galaxy and compared, where possible, our data with that previously produced by the *IRAS*, *ISO*, *Spitzer* and *Planck*. Table 1 gives a complete list of the galaxies in the sample and their flux densities in each far-infrared band.

These flux densities enable us to make a measurement of the luminosity function/distribution in each band. These luminosity function/distributions are not power laws but 'peaked' functions. If subsequent measurements of the luminosity distributions in more wide-ranging environments have the more common power-law form (Schechter), then this is a clear indication of environmental processes in the cluster affecting the far-infrared properties of galaxies.

We define and measure for each galaxy a 100–500 μm far-infrared and an optical 0.4–2.5 μm luminosity ($L_{100-500}$ and $L_{0.4-2.5}$, respectively). Assuming a simple screen model of dust, these luminosities can be used to calculate a 'typical' optical depth ($\langle\tau\rangle$) for photons emerging from a galaxy. Values of $\langle\tau\rangle$ range from zero to an optically thick 2.8. With a mean value of $\langle\tau_{\rm mean}\rangle = 0.4$, most cluster (stellar) photons are emerging from reasonably optically-thin optical depths. We also use the values of $L_{100-500}$ and $L_{0.4-2.5}$ for each galaxy to calculate far-infrared and optical luminosity densities of $[1.6(7.0) \pm 0.2] \times 10^9$ $L_\odot$ Mpc^{-3} and $5.0(20.0) \times 10^9$ $L_\odot$ Mpc^{-3}, respectively. The optical luminosity density is some 3.2(2.9) times larger than the far-infrared one.

The derived flux densities in each band are also used to calculate a dust mass and temperature for each galaxy, assuming a single-component modified blackbody with $\beta = 2$. The mean (typical) dust mass and temperature for the galaxies in this sample are $\log(M_{\rm Dust}) = 7.31$ and $T_{\rm D} = 20.0$ K, respectively. We have also used data from the literature to calculate both stellar and atomic gas masses for each galaxy; these have mean values of $\log(M_{\rm stars}) = 10.26$ and $\log(M_{\rm H\,I}) = 9.08$, respectively. The total masses in each of these baryonic components are used to calculate mass densities of $8.6(27.8) \times 10^6$, $4.6(13.9) \times 10^8$ and $7.8(29.7) \times 10^9$ $M_\odot$ Mpc^{-3} for cluster dust, atomic gas and stars, respectively. These values are higher than that derived using galaxies in the general field by factors of 39(126), 6(18) and 34(129), respectively. Atomic gas appears to have been lost or consumed more effectively than is typical in field galaxies.

The above information on the properties of Virgo Cluster galaxies and on the properties of the cluster as a whole will hopefully be useful when compared with the global properties of galaxies throughout the local Universe and also with studies of other galaxy clusters both near and far.

ACKNOWLEDGMENTS

The *Herschel* spacecraft was designed, built, tested and launched under a contract to the ESA managed by the Herschel/Planck Project team by an industrial consortium under the overall responsibility of the prime contractor Thales Alenia Space (Cannes), and including Astrium (Friedrichshafen) responsible for the payload module and for system testing at spacecraft level, Thales Alenia Space (Turin) responsible for the service module, and Astrium (Toulouse) responsible for the telescope, within excess of a hundred subcontractors.

The PACS has been developed by a consortium of institutes led by the MPE (Germany) and including UVIE (Austria); KU Leuven, CSL, IMEC (Belgium); CEA, LAM (France); MPIA (Germany); INAF-IFSI/OAA/OAP/OAT, LENS, SISSA (Italy); and IAC (Spain). This development has been supported by the funding agencies BMVIT (Austria), ESA-PRODEX (Belgium), CEA/CNES (France), DLR (Germany), ASI/INAF (Italy) and CICYT/MCYT (Spain).

The SPIRE has been developed by a consortium of institutes led by Cardiff University (UK) and including University of Lethbridge (Canada); NAOC (China); CEA, LAM (France); IFSI, University of Padua (Italy); IAC (Spain); Stockholm Observatory (Sweden); Imperial College London, RAL, UCL-MSSL, UKATC, University of Sussex (UK); and Caltech, JPL, NHSC, University of Colorado (USA). This development has been supported by national funding agencies: CSA (Canada); NAOC (China); CEA, CNES, CNRS (France); ASI (Italy); MCINN (Spain); SNSB (Sweden); STFC (UK); and NASA (USA).

This research has made use of the NED which is operated by the Jet Propulsion Laboratory, California Institute of Technology, under contract with NASA.

Funding for the SDSS and SDSS-II has been provided by the Alfred P. Sloan Foundation, the Participating Institutions, the National Science Foundation, the US Department of Energy, NASA, the Japanese Monbukagakusho, the Max Planck Society, and the Higher Education Funding Council for England. The SDSS website is http://www.sdss.org/. The SDSS is managed by the Astrophysical Research Consortium for the Participating Institutions. The Participating Institutions are the American Museum of Natural History, Astrophysical Institute Potsdam, University of Basel, University of Cambridge, Case Western Reserve University, University of Chicago, Drexel University, Fermilab, the Institute for Advanced Study, the Japan Participation Group, The Johns Hopkins University, the Joint Institute for Nuclear Astrophysics, the Kavli Institute for Particle Astrophysics and Cosmology, the Korean Scientist Group, the Chinese Academy of Sciences (LAMOST), Los Alamos National Laboratory, the Max Planck Institute for Astronomy (MPIA), the Max Planck Institute for Astrophysics (MPA), New Mexico State University, Ohio State University, University of Pittsburgh, University of Portsmouth, Princeton University, the United States Naval Observatory and the University of Washington.

This publication makes use of data products from the 2MASS, which is a joint project of the University of Massachusetts and the Infrared Processing and Analysis Center/California Institute of Technology, funded by NASA and the National Science Foundation.

SB, LM, CP, LKH, SdiSA, EC and GG acknowledge the financial support by the ASI through the ASI-INAF grant 'HeViCS: the Herschel Virgo Cluster Survey' I/009/10/0.

This work received support from the ALMA-CONICYT Fund for the Development of Chilean Astronomy (Project 31090013) and from the Center for Excellence in Astrophysics and Associated Technologies (PBF 06).

REFERENCES

Abazajian K. et al., 2009, ApJS, 182, 543
Alton P. et al., 1998a, A&A, 335, 807
Alton P., Bianchi S., Rand R., Xilouris E., Davies J., Trewhella M., 1998b, ApJ, 507, L125
Babbedge T. et al., 2006, MNRAS, 370, 1159
Baes M., Dejonghe H., 2001, MNRAS, 326, 733
Baes M., Clemens M., Xilouris E. et al., 2010, A&A, 518, 53
Baldry K., Glazebrook K., Driver S., 2008, MNRAS, 388, 945
Bell E., McIntosh Daniel H., Katz N., Weinberg M., 2003, ApJS, 149, 289
Bendo G. et al., 2002, AJ, 123, 3067
Bendo G. et al., 2003, AJ, 125, 2361
Bendo G. et al., 2010, A&A, 518, 65
Bendo G. et al., 2011, preprint (astro-ph/1109.0237)
Bertin E., Arnouts S., 1996, A&AS, 117, 393
Bianchi S., 2008, A&A, 490, 461
Bianchi S., Davies J., Alton P., 2000a, A&A, 359, 65
Bianchi S., Davies J., Alton P., Gerin M., Casoli F., 2000b, A&A, 353, 13
Bicay M., Giovanelli R., 1987, ApJ, 321, 645
Binggeli B., Sandage A., Tammann G., 1985, AJ, 90, 1681
Binggeli B., Tammann G., Sandage A., 1987, AJ, 94, 251
Boehringer H., Briel U., Schwarz R., Voges W., Hartner G., Trumper J., 1994, Nat, 368, 828
Boselli A., Gavazzi G., 2006, PASP, 118, 517
Boselli A. et al., 2010, A&A, 518, 61
Boselli A. et al., 2011, A&A, 528, 107
Calzetti D. et al., 2010, ApJ, 714, 1256

Chung A., van Gorkom J., Kenney J., Crowl H., Vollmer B., 2009, AJ, 138, 1741
Clemens M. et al., 2010, A&A, 518, 50
Cortese L., Davies J., Baes M. et al., 2010, A&A, 518, 49
Cortese L., Catinella B., Boissier S., Boselli A., Heinis S., 2011, MNRAS, 415, 1797
Davies J., Alton P., Trewhella M., Evans R., Bianchi S., 1999, MNRAS, 304, 495
Davies J. et al., 2004, MNRAS, 349, 922
Davies J. et al., 2010, A&A, 518, 48
Davies J. et al., 2011, MNRAS, 415, 1883
De Looze I. et al., 2010, A&A, 518, 54
Devereux N., Young J., 1990, ApJ, 359, 42
Dowell C. et al., 2010, in Oschmann J., Clampin M., MacEwen H., eds, Proc. SPIE Vol. 7731, Space Telescopes and Instrumentation, p. 36
Doyon R., Joseph R., 1989, MNRAS, 239, 347
Draine B., 2003, ARA&A, 41, 241
Draine B. et al., 2007, ApJ, 663, 866
Dunne L., Eales S., Edmunds M., Ivison R., Alexander P., Clements D., 2000, MNRAS, 315, 115
Dunne L. et al., 2011, MNRAS, 417, 1510
Dwek E., 1998, ApJ, 501, 643
Eales S. et al., 2010, PASP, 122, 499
Edmunds M., Eales S., 1998, MNRAS, 299, L29
Gavazzi G., Boselli A., Scodeggio M., Pierini D., Belsole E., 1999, MNRAS, 304, 595
Gavazzi G., Boselli A., Donati A., Franzetti P., Scodeggio M., 2003, A&A, 400, 451
Giovanelli R. et al., 2005, AJ, 130, 2598
Gomez P. et al., 2003, ApJ, 584, 210
Griffin M. et al., 2009, EAS Publ. Ser., 34, 33
Griffin M. et al., 2010, A&A, 518, 3
Grossi M. et al., 2010, A&A, 518, 52
Haynes M., Giovanelli R., 1984, AJ, 89, 758
Ibar E. et al., 2010, MNRAS, 409, 38
Kennicutt R. C., Jr, et al., 2003, PASP, 115, 928
Kent B. et al., 2007, ApJ, 665, 15
Lewis I. et al., 2002, MNRAS, 334, 673
Magrini L. et al., 2011, A&A, 535, 13
Martin A., Papastergis E., Giovanelli R., Haynes M., Springob C., Stierwalt S., 2010, ApJ, 723, 1559
Mei S. et al., 2007, ApJ, 655, 144
Mei S. et al., 2010, BAAS, 42, 514
Neugebauer G. et al., 1984, ApJ, 278, L1
Ott S., 2010, in Mizumoto Y., Morita K. I., Ohishi M., eds, ASP Conf. Ser. Vol. 434, Astronomical Data Analysis Software and Systems XIX. Astron. Soc. Pac., San Francisco, p. 139
Pilbratt G. et al., 2010, A&A, 518, 1
Poglitsch A. et al., 2010, A&A, 518, 2
Popescu C., Tuffs R., 2002, MNRAS, 335, L41
Popescu C., Tuffs R., Volk H., Pierini D., Madore B., 2002, AJ, 567, 221
Rodighiero G. et al., 2010, A&A, 515, 8
Rowan-Robinson M., Helou G., Walker D., 1987, MNRAS, 227, 589
Sabatini et al., 2003, MNRAS, 341, 981
Sandage A., Binggeli B., Tammann G., 1985, AJ, 90, 1759
Saunders W., Rowan-Robinson M., Lawrence A., Efstathiou G., Kaiser N., Ellis R., Frenk C., 1990, MNRAS, 242, 318
Skrutskie M. et al., 2006, AJ, 131, 1163
Smith M., Vlahakis C., Baes M. et al., 2010, A&A, 518, 51
Soifer B. et al., 1987, ApJ, 320, 238
Stickel M., Lemke D., Mattila K., Haikala L., Haas M., 1998, A&A, 329, 55
Stickel M., Lemke D., Klaas U., Krause O., Egner S., 2004, A&A, 422, 39S
Swinyard B. et al., 2010, A&A, 518, 4
Takeuchi T., Ishii T., Dole H., Dennefeld M., Lagache G., Puget J., 2006, A&A, 448, 525
Taylor R., 2010, PhD thesis, Cardiff University
Trewhella M., Davies J., Alton P., Bianchi S., Madore B., 2000, ApJ, 543, 153
Tuffs R. et al., 2002, ApJS, 139, 37
Vlohakis C., Dunne L., Eales S., 2005, MNRAS, 364, 1253
Warren S. et al., 2007, MNRAS, 375, 213

This paper has been typeset from a TEX/LATEX file prepared by the author.